

## ABSTRACT

We propose a non-linear gravity inversion for simultaneously estimating the basement and Moho geometries, as well as the depth of the reference Moho along a profile crossing a passive rifted margin. We approximate the subsurface by an interpretation model composed of four layers. The shallowest represents water and has constant density contrast. The second has a number of sub-layers with constant density contrasts. The complexity of this layer depends on the available a priori information at the study area. The third layer represents the crust and has a predefined horizontal density variation along the profile. Finally, the deepest layer represents the mantle, with constant density contrast. Top and base of third layer represent the basement and Moho, respectively. The constant depth defining the base of the interpretation model defines the reference Moho. To obtain stable solutions, we impose smoothness on basement and Moho, force them to be close to previously estimated depths along the profile and also impose local isostatic equilibrium. Differently from previous methods, we introduce the information of local isostatic equilibrium by imposing smoothness on the lithostatic stress exerted at depth. Our method allows deviations from isostatic equilibrium along the profile, so that the interpreter can obtain a set of candidate models that fit the observed data and exhibit different degrees of isostatic equilibrium. Tests with synthetic data show the good performance of our method at regions with pronounced crustal thinning, which is typical of passive volcanic margins. Results obtained at the Pelotas basin, an example of passive volcanic margin at the southern of Brazil, agree with a previous interpretation obtained independently by using seismic data. These results show that, combined with a priori information, our method is a promising tool for interpreting gravity data on passive rifted margins.

## INTRODUCTION

Gravity methods have long been used to investigate the crustal structure in local studies. A common approach is approximate the crust by a set of juxtaposed layers with constant or depth-dependent density distributions. The boundaries of these juxtaposed layers are defined by surfaces that generally represent sedimentary layers, bathymetry, relief of basement or the Mohorovicic discontinuity (or simply Moho). Here, we consider methods that estimate the geometry of these surfaces. There is a large group of methods estimating the geometry of a single surface representing the basement relief in the space domain (e.g., Bott, 1960; Tanner, 1967; Cordell and Henderson, 1968; Barbosa et al., 1997, 1999b,a; Condi et al., 1999; Silva et al., 2006; Chakravarthi and Sundararajan, 2007; Martins et al., 2010; Silva et al., 2010; Lima et al., 2011; Martins et al., 2011; Barnes and Barraud, 2012; Silva et al., 2014; Silva and Santos, 2017), and the Fourier domain (e.g., Oldenburg, 1974; Granser, 1987; Reamer and Ferguson, 1989; Guspí, 1993). Another group of methods estimate a single surface representing the Moho in the space domain (e.g., Shin et al., 2009; Bagherbandi and Eshagh, 2012; Barzaghi and Biagi, 2014; Sampietro, 2015; Uieda and Barbosa, 2017) and in the Fourier domain (e.g., Braitenberg et al., 1997; Braitenberg and Zadro, 1999; van der Meijde et al., 2013). Finally, there is a small group of methods estimating the geometry of multiple surfaces (e.g., Braitenberg et al., 2003; Camacho et al., 2011; Salem et al., 2014; Ferderer et al., 2017; García-Abdeslem, 2017; Salem, 2017).

All these methods suffer from the inherent ambiguity (Skeels, 1947; Roy, 1962) in determining the true physical property distribution that produces a discrete set of observed gravity data. It is well known that, by presuming a fixed density distribution for each layer, it is possible to find different surfaces producing the same gravity data. It is known that

methods estimating multiple surfaces suffer from a greater ambiguity if compared with those estimating the geometry of a single surface. This inherent ambiguity is drastically increased for the cases in which, besides the geometry of the surfaces, the density distribution of the layers are also estimated. To partially overcome the ambiguity and generate meaningful solutions, the interpreter must use a priori information obtained from seismic data and/or boreholes in order to constrain the range of possible models. Some authors opted for combining gravity data with seismic and isostasy to reduce this inherent ambiguity. As properly pointed out by Gradmann et al. (2017), isostasy is equally sensitive to shallow and deep structures. This characteristic makes it a powerful tool to validate interpretations of deep seismic data and gravity models.

Condi et al. (1999) proposed a nonlinear gravity inversion for estimating the offshore deep structures of a rifted margin. Their method uses local isostasy for directly constraining the geometries of the shallow and deeper parts of their model, without necessarily forcing it to be in a perfect isostatic equilibrium. Braitenberg et al. (2003) proposed a method for estimating the bathymetry and Moho geometries from gravity data by imposing regional isostatic equilibrium in the frame of the thin-plate isostatic flexure model over an oceanic basin. Salem et al. (2014) presented a non-linear gravity inversion for estimating the surfaces representing basement and Moho on an onshore rifted basin. The basement relief is by using an iterative approach similar to that presented by Bott (1960) and Cordell and Henderson (1968). The difference is that, at each iteration, the Airy-Heiskanen model (Heiskanen and Moritz, 1967, p. 135) for local isostatic equilibrium is used to subsequently update the Moho geometry, forcing the model to be in perfect isostatic equilibrium according to the Airy-Heiskanen model. Notice that their method does not estimate the geometries of basement and Moho simultaneously. As properly pointed out by Silva et al. (2014),

Bott’s method does not define optimal step sizes at the iterative corrections, does not impose constraints for obtaining stable solutions, nor use an objective stopping criterion. Consequently, the method presented by Salem et al. (2014) is also susceptible to these limitations. García-Abdeslem (2017) uses an approach based on flexural isostasy to estimate the Moho and compute a regional gravity field, which is subsequently subtracted from the observed gravity data to obtain a residual gravity field. His method consists in solving a non-linear inverse problem for estimating the basement geometry explaining the residual gravity field. Salem (2017) presents a general framework for estimating the surfaces associated with basement and Moho on a rifted continental margin. His method is based on an empirical logistic function that acts as a gain control of the Moho uplift and introduces information about isostatic equilibrium by correlating the gravity data produced by the basement and Moho. Similarly to Salem et al. (2014) and García-Abdeslem (2017), the method presented by Salem (2017) does not estimate the surfaces of basement and Moho simultaneously. The Moho surface is estimated in a first step and then used to estimate the basement surface. Ferderer et al. (2017) proposed a “general local isostasy” approach, which consists in combining the Airy-Heiskanen and Pratt-Hayford models (Heiskanen and Moritz, 1967) so that the crust density and geometry may vary laterally in order to maintain the local isostatic equilibrium on a profile crossing a rifted margin. Their approach also uses local isostasy to directly link the geometries of shallow and deeper structures with the purpose of reducing the range of possible solutions. They propose a method for estimating the geometries of basement and Moho and density contrasts by using a grid-search technique (Sen and Stoffa, 2013). Such techniques involve the systematic search for model parameters producing the best data fit and may be far from being practical in geophysical applications for the cases in which the model space is very large and the forward problem is slow.

We present a non-linear gravity inversion method for simultaneously estimating the geometries of basement and Moho, as well as a constant depth representing a reference Moho along a profile crossing a rifted margin. Our method is formulated, in the space domain, as a non-linear gravity inversion based on the Levenberg-Marquardt method (Silva et al., 2001; Aster et al., 2005), by following the same strategy of Barbosa et al. (1999b) to incorporate inequality constraints. The parameters to be estimated are the constant depth representing the reference Moho and the geometries of basement and Moho. At each iteration, our method simultaneously estimates corrections for the reference Moho, as well as the geometries of basement and Moho. In order to produce stable solutions, we use different constraints imposing smoothness on basement and Moho surfaces. Additionally, we force them to be close to some depths along the profile.

Similarly to Ferderer et al. (2017), we combine the Airy-Heiskanen and Pratt-Hayford models to impose local isostatic equilibrium. However, there are three significant differences between our approach and those presented in earlier studies. The first one is the way we impose isostatic equilibrium. Differently from previous methods, we do not use local isostasy to directly link the geometries of basement and Moho. Rather, we impose smoothness on the lithostatic stress exerted by the interpretation model on a constant compensation depth, below which there are no lateral density variations. This information is directionally consistent with the basic principle of local isostatic equilibrium according to the Airy-Heiskanen and Pratt-Hayford models. Our constraint introduces the information that the lithostatic stress must be mostly smooth along the entire profile, except at some isolated regions, where it can present abrupt variations. At these regions, our method enables the estimated model to deviate from the local isostatic equilibrium. This is particularly useful at margins showing pronounced crustal thinning. The second aspect by which our

approach differs from those in the literature is that it allows the interpreter to control how much the estimated models can deviate from the isostatic equilibrium. As a consequence, the interpreter can obtain a set of candidate models that (i) fit the observed data and (ii) present different degrees of isostatic equilibrium. Finally, it is worth noting that, in contrast to most of earlier studies, our method attempts to use isostasy for exploring (and not necessarily reducing) the inherent ambiguity of gravity methods.

Tests with synthetic data show the good performance of our method in simultaneously retrieving the geometry of basement and Moho of a realistic margin model, which is based on a seismic profile crossing the East Greenland margin, over the Jameson Land basin (Peron-Pinvidic et al., 2013), and shows an extreme crustal thinning. We also applied our method to invert gravity data on a profile over the Pelotas basin (Stica et al., 2014). This basin is located at the offshore southern of Brazil and is considered a classical example of volcanic passive margin (Geoffroy, 2005). We inverted gravity data provided by the combined global gravity field model EIGEN-6C4 (Förste et al., 2014), one of the latest releases of the “European Improved Gravity model of the Earth by New techniques” series. Our results are consistent with the models presented by Stica et al. (2014) and Zalán (2015), who combined seismic, gravity and magnetic data. These results show that, combined with a priori information, simple isostatic models can be helpful in investigating continental margins, specially at regions presenting pronounced crustal thinning.

## METHODOLOGY

### Forward problem

Let  $\mathbf{d}^o$  be the observed data vector, whose  $i$ -th element  $d_i^o$ ,  $i = 1, \dots, N$ , represents the observed gravity disturbance (Heiskanen and Moritz, 1967) at the point  $(x_i, y_i, z_i)$ , on a profile located over a rifted passive margin. The coordinates are referred to a topocentric Cartesian system, with  $z$ -axis pointing downward,  $y$ -axis along the profile and  $x$ -axis perpendicular to the profile. In local- and regional-scale studies, the gravity disturbance represents the vertical component of the gravitational attraction exerted by the gravity sources. It is more appropriated for geophysical applications, numerically similar to the classical free-air anomaly and uses the height relative to the reference ellipsoid (geometric height) instead of the Geoid (orthometric height) (Li and Götze, 2001; Fairhead et al., 2003; Hackney and Featherstone, 2003; Hinze et al., 2005; Vajda et al., 2006, 2007).

The density distribution in a rifted margin can be very complex. In volcanic margins, for example, the crust may consist partially or wholly of flood-basalts and tuffs, which are commonly imaged as Seaward Dipping Reflectors (SDR). Underneath this intruded crust, high-velocity seismic zones are usually interpreted as bodies of underplated mafic to ultra-mafic magma (Geoffroy, 2005). We assume that the actual mass distribution in a rifted passive margin can be schematically represented according to Figure 1. In this model, the subsurface is formed by four layers. Layer 1 is the shallowest and represents a water layer with constant density  $\rho^{(w)}$ . Layer 2 is formed by  $Q$  vertically adjacent sub-layers representing sediments, salt or volcanic rocks. In our example, this layer is formed by two sub-layers with constant densities  $\rho^{(q)}$ ,  $q = 1, 2$ . Different models can be created by changing the number  $Q$  according to the complexity of the study area and available a priori

information. In many cases, seismic data can be used to constrain the geometry of these shallow structures. Layer 3 represents the crust and we presume that its density  $\rho^{(c)}$  varies horizontally along the profile, according to a predefined function. In Figure 1, we consider that crust density assumes two possible values. It can be equal to  $\rho^{(cc)}$ , which represents the continental crust, or equal to  $\rho^{(oc)}$ , which represents the oceanic crust. However, more complex functions representing the crust density distribution can be specified according to interpreter’s knowledge about the geology at study area. This approach presumes that bulk values can be used to approximate the real density distribution at the deeper parts of crust. Finally, Layer 4 represents a homogeneous mantle with constant density  $\rho^{(m)}$ . The surface separating the Layers 2 and 3 defines the basement relief whereas that separating Layers 3 and 4 defines the Moho. These surfaces are represented as dashed-white lines in Figure 1.

In order to define the anomalous mass distribution producing the observed gravity disturbance, we presume a reference mass distribution formed by two layers. The shallowest represents a homogeneous crust with constant density  $\rho^{(r)}$ . Its thickness is schematically represented in Figure 1. The deepest layer in the reference mass distribution represents a homogeneous mantle with constant density  $\rho^{(m)}$ . Notice that the mantle in the reference mass distribution has the same density as the mantle in our rifted margin model (Figure 1). The surface separating the crust and mantle in the reference mass distribution is conveniently called *reference Moho* (Figures 1 and 2). The reference model can be thought of as the outer layers of a concentric mass distribution producing the normal gravity field. In a local scale, this concentric mass distribution is close to a stack of two Bouguer slabs.

We consider that the anomalous mass distribution producing the observed data is defined as the difference between the rifted margin model and the reference mass distribution (Figure 1). As a consequence, the anomalous mass distribution is characterized by re-



gions with constant density contrasts. This anomalous distribution is approximated by an interpretation model formed by  $N$  columns of vertically stacked prisms (Figure 2). For convenience, we presume that there is an observed gravity disturbance over the center of each column. We consider that the prisms in the extremities of the interpretation model extend to infinity along the  $y$ -axis in order to prevent edge effects in the forward calculations. The  $i$ -th column is formed by vertically stacked prisms having infinite length along the  $x$ -axis and locally approximates the four layers of our rifted margin model (Figure 1).

Layer 1 is defined by a single prism, has thickness  $t_i^{(w)}$  and a constant density contrast  $\Delta\rho^{(w)} = \rho^{(w)} - \rho^{(r)}$ . Layer 2 is defined by the interpreter, according to the complexity of the study area and the available a priori information, by a set of  $Q$  vertically stacked prisms, each one with thickness  $t_i^{(q)}$  and constant density contrast  $\Delta\rho^{(q)} = \rho^{(q)} - \rho^{(r)}$ ,  $q = 1, \dots, Q$ . Layer 3 represents the deeper part of the crust, it is also formed by a single prism, has thickness  $t_i^{(c)}$  and density contrast  $\Delta\rho_i^{(c)} = \rho_i^{(c)} - \rho^{(r)}$ , with  $\rho_i^{(c)}$  being the crust density at the coordinate  $y_i$ ,  $i = 1, \dots, N$ , along the profile. According to Figure 2, the crust density contrast  $\Delta\rho_i^{(c)}$  may assume two possible values, depending on its position with respect to the coordinate  $y_{COT}$  of the Crust-Ocean Transition (COT). More complex models can be set by the interpreter according to the available a priori information at the study area. The top and bottom of this layer define, respectively, the basement and Moho. Finally, Layer 4 representing the mantle is divided into two sub-layers, each one formed by a single prism having the same constant density contrast  $\Delta\rho^{(m)} = \rho^{(m)} - \rho^{(r)}$ . The shallowest sub-layer has thickness  $t_i^{(m)}$ . Its top and bottom define, respectively, the depths of Moho and the compensation depth  $S_0$ . The deepest sub-layer has thickness  $\Delta S$ , top at  $S_0$  and bottom at  $S_0 + \Delta S$ , which defines the reference Moho.

Given the density contrasts, the COT position  $y_{COT}$ , the compensation depth  $S_0$ , the

thickness  $t_i^{(w)}$  of the prisms defining Layer 1 and also the thickness  $t_i^{(q)}$ ,  $i = 1 \dots, N$ , of the prisms forming the upper  $Q - 1$  sub-layers of Layer 2, it is possible to describe the interpretation model in terms of an  $M \times 1$  parameter vector  $\mathbf{p}$ ,  $M = 2N + 1$ , defined as follows:

$$\mathbf{p} = \begin{bmatrix} \mathbf{t}^{(Q)} \\ \mathbf{t}^{(m)} \\ \Delta S \end{bmatrix}, \quad (1)$$

where  $\mathbf{t}^{(Q)}$  and  $\mathbf{t}^{(m)}$  are  $N \times 1$  vectors whose  $i$ -th elements  $t_i^{(Q)}$  and  $t_i^{(m)}$  (Figure 2) represent the thickness of the prisms forming, respectively, the base of Layer 2 and the top of Layer 4. Notice that  $t_i^{(Q)}$  and  $t_i^{(m)}$ ,  $i = 1, \dots, N$ , approximate, respectively, the geometries of basement and Moho and  $\Delta S$  defines the depth of the reference Moho (Figure 2). In this case, the gravity disturbance produced by the interpretation model (the predicted gravity disturbance) at the position  $(x_i, y_i, z_i)$  can be written as the sum of the vertical component of the gravitational attraction exerted by the  $L$  prisms forming the interpretation model as follows:

$$d_i(\mathbf{p}) = k_g G \sum_{j=1}^L f_{ij}(\mathbf{p}), \quad (2)$$

where  $f_{ij}(\mathbf{p})$  represents an integral over the volume of the  $j$ -th prism. Here, these volume integrals are computed with the expressions proposed by Nagy et al. (2000), by using the open-source Python package *Fatiando a Terra* (Uieda et al., 2013).

## Inverse problem formulation

Let  $\mathbf{d}(\mathbf{p})$  be the predicted data vector, whose  $i$ -th element  $d_i(\mathbf{p})$  is the vertical component of the gravitational attraction (equation 2) exerted by the interpretation model at the position  $(x_i, y_i, z_i)$  on the profile. We estimate a particular parameter vector producing a predicted

data  $\mathbf{d}(\mathbf{p})$  as close as possible to the observed data  $\mathbf{d}^o$  by minimizing the goal function

$$\Gamma(\mathbf{p}) = \Phi(\mathbf{p}) + \sum_{\ell=0}^4 \mu_{\ell} \Psi_{\ell}(\mathbf{p}) , \quad (3)$$

subject to the inequality constraint

$$p_j^{min} < p_j < p_j^{max} , \quad j = 1, \dots, M , \quad (4)$$

where  $p_j^{min}$  and  $p_j^{max}$  define, respectively, lower and upper bounds for the  $j$ -th element of  $\mathbf{p}$ .

In equation 3,  $\mu_{\ell}$  is the weight assigned to the  $\ell$ -th regularizing function  $\Psi_{\ell}(\mathbf{p})$ ,  $\ell = 0, \dots, 4$ ,

and  $\Phi(\mathbf{p})$  is the misfit function given by

$$\Phi(\mathbf{p}) = \frac{1}{N} \|\mathbf{d}^o - \mathbf{d}(\mathbf{p})\|_2^2 , \quad (5)$$

where  $\|\cdot\|_2^2$  represents the squared Euclidean norm. Notice that our method estimates the parameter vector  $\mathbf{p}$  (equation 1), which contains the geometries of basement and Moho, as well as the thickness  $\Delta S$  defining the depth of the reference Moho (Figure 2). The bottom of Layer 1 is defined by the available bathymetry. The geometry of the upper sub-layers forming Layer 2 and the constant compensation depth  $S_0$  (Figure 2) are defined by using the available a priori information. These predefined quantities remain fixed during the inversion. Details about the regularizing functions  $\Psi_{\ell}(\mathbf{p})$ ,  $\ell = 0, \dots, 4$  and the numerical procedure to solve this non-linear inverse problem are given in the following sections.

### Isostatic constraint

Consider that no vertical forces are acting on the lateral surfaces of each column forming the model (Figure 2). In this case, the lithostatic stress (pressure)  $\tau_i$  (in MPa) exerted by the  $i$ -th column at the surface  $S_0$  can be computed according to the Archimedes' principle

as follows (Turcotte and Schubert, 2002, p. 129):

$$t_i^{(w)} \rho^{(w)} + t_i^{(1)} \rho_i^{(1)} + \dots + t_i^{(Q)} \rho_i^{(Q)} + t_i^{(c)} \rho_i^{(c)} + t_i^{(m)} \rho^{(m)} = \tau_i g_m^{-1}, \quad (6)$$

where  $g_m$  is the mean gravity value on the study area. We consider this mean value equal to  $9.81 \text{ m/s}^2$  along the profile. By rearranging terms in equation 6 and using the relation

$$S_0 = t_i^{(w)} + t_i^{(1)} + \dots + t_i^{(Q)} + t_i^{(c)} + t_i^{(m)}, \quad (7)$$

it is possible to show that:

$$\Delta \tilde{\rho}_i^{(Q)} t_i^{(Q)} + \Delta \tilde{\rho}_i^{(m)} t_i^{(m)} + \Delta \tilde{\rho}_i^{(w)} t_i^{(w)} + \Delta \tilde{\rho}_i^{(1)} t_i^{(1)} + \dots + \Delta \tilde{\rho}_i^{(Q-1)} t_i^{(Q-1)} + \rho_i^{(c)} S_0 = \tau_i g_m^{-1}, \quad (8)$$

where  $\Delta \tilde{\rho}_i^{(\alpha)} = \rho_i^{(\alpha)} - \rho_i^{(c)}$ ,  $\alpha = w, 1, \dots, Q-1, Q, m$ . In order to describe the lithostatic stress exerted by all columns forming the interpretation model on the surface  $S_0$ , equation 8 can be written as follows:

$$\mathbf{M}^{(Q)} \mathbf{t}^{(Q)} + \mathbf{M}^{(m)} \mathbf{t}^{(m)} + \mathbf{M}^{(w)} \mathbf{t}^{(w)} + \mathbf{M}^{(1)} \mathbf{t}^{(1)} + \dots + \mathbf{M}^{(Q-1)} \mathbf{t}^{(Q-1)} + \boldsymbol{\rho}^{(c)} S_0 = g_m^{-1} \boldsymbol{\tau}, \quad (9)$$

where  $\boldsymbol{\tau}$  is an  $N \times 1$  vector whose  $i$ -th element is the  $\tau_i$  (equation 6) associated with the  $i$ -th column;  $\mathbf{t}^{(\alpha)}$ ,  $\alpha = w, 1, \dots, Q-1, Q, m$ , is an  $N \times 1$  vector with  $i$ -th element defined by the thickness  $t_i^{(\alpha)}$  of a prism in the  $i$ -th column;  $\mathbf{M}^{(\alpha)}$  is an  $N \times N$  diagonal matrix whose elements are defined by the density contrasts  $\Delta \tilde{\rho}_i^{(\alpha)}$ ,  $i = 1, \dots, N$ , of the prisms in a layer and  $\boldsymbol{\rho}^{(c)}$  is an  $N \times 1$  vector containing the densities of the prisms representing the crust. The term  $g_m^{-1} \boldsymbol{\tau}$  describing the lithostatic stress exerted by all prisms on  $S_0$  is conveniently called *lithostatic stress curve*.

Let us now use an approach similar to that presented by Ferderer et al. (2017) to combine the Airy-Heiskanen and Pratt-Hayford models (Heiskanen and Moritz, 1967) in order to impose local isostatic equilibrium. We impose this condition by varying both density and

geometry of the crust along the rifted margin. In this case, the lithostatic stress exerted by the interpretation model must be constant at the compensation depth  $S_0$  (Figure 2). Differently from previous approaches in literature, we impose isostatic equilibrium by forcing the lithostatic stress to be smooth at  $S_0$ . We apply the first-order Tikhonov regularization (Aster et al., 2005) to the lithostatic stress curve  $g_m^{-1} \boldsymbol{\tau}$  (equation 9), obtaining the following expression:

$$\mathbf{R}(\mathbf{C}\mathbf{p} + \mathbf{D}\mathbf{t}) = \mathbf{0}, \quad (10)$$

where  $\mathbf{0}$  is a vector with null elements and the remaining terms are given by:

$$\mathbf{C} = \begin{bmatrix} \mathbf{M}^{(Q)} & \mathbf{M}^{(m)} & \mathbf{0} \end{bmatrix}_{N \times M}, \quad (11)$$

$$\mathbf{D} = \begin{bmatrix} \mathbf{M}^{(w)} & \mathbf{M}^{(1)} & \dots & \mathbf{M}^{(Q-1)} & \boldsymbol{\rho}^{(c)} \end{bmatrix}_{N \times (QN+1)}, \quad (12)$$

$$\mathbf{t} = \begin{bmatrix} \mathbf{t}^{(w)} \\ \mathbf{t}^{(1)} \\ \vdots \\ \mathbf{t}^{(Q-1)} \\ S_0 \end{bmatrix}_{(QN+1) \times 1}, \quad (13)$$

and  $\mathbf{R}$  is an  $(N-1) \times N$  matrix, whose element  $ij$  is defined as follows:

$$[\mathbf{R}]_{ij} = \begin{cases} 1 & , \quad j = i \\ -1 & , \quad j = i + 1 \\ 0 & , \quad \text{otherwise} \end{cases}. \quad (14)$$

Finally, from equation 10, it is possible to define the regularizing function  $\Psi_0(\mathbf{p})$  (equation 3):

$$\Psi_0(\mathbf{p}) = \|\mathbf{W}\mathbf{R}(\mathbf{C}\mathbf{p} + \mathbf{D}\mathbf{t})\|_2^2, \quad (15)$$

where  $\mathbf{W}$  is an  $(N - 1) \times (N - 1)$  diagonal matrix having constant elements  $0 < w_{ii} \leq 1$ ,  $i = 1, \dots, N - 1$ . Function  $\Psi_0(\mathbf{p})$  defines the *Isostatic constraint*.

Notice that, by minimizing the function  $\Psi_0(\mathbf{p})$  (equation 15), the method imposes smoothness on the lithostatic stress exerted by the interpretation model on the compensation depth  $S_0$ . Matrix  $\mathbf{W}$  controls the relative amount of isostatic equilibrium imposed along the profile. In the particular case in which all diagonal elements  $w_{ii}$  have the same constant value, the same amount of isostatic equilibrium is imposed along the whole profile. On the other hand, different amounts of isostatic equilibrium can be imposed along the profile by varying the values of these elements. Elements  $w_{ii} \approx 1$  impose a smooth lithostatic stress curve at the transition between columns  $i$  and  $i + 1$  of the interpretation model. Elements  $w_{ii} \approx 0$  allow abrupt variations in the lithostatic stress curve between columns  $i$  and  $i + 1$  of the interpretation model. By using all elements  $w_{ii} = 1$ , we impose full isostatic equilibrium along the entire profile. Alternatively, we may enable the interpretation model to deviate from the isostatic equilibrium by conveniently decreasing the numerical values assigned to the elements  $w_{ii}$  at specific regions along the profile. The strategy used to define the elements  $w_{ii}$  is presented in the specific section describing the computational procedures for solving the inverse problem.

## Smoothness constraints

These constraints impose smoothness on the adjacent thickness of the prisms defining the geometries of basement (base of Layer 2) and Moho (top of Layer 4). This information is introduced by applying the first-order Tikhonov regularization (Aster et al., 2005) to the vectors  $\mathbf{t}^{(Q)}$  and  $\mathbf{t}^{(m)}$  (equation 1). Mathematically, these constraints are represented by

the regularizing functions  $\Psi_1(\mathbf{p})$  and  $\Psi_2(\mathbf{p})$  (equation 3), which are given by:

$$\Psi_1(\mathbf{p}) = \|\mathbf{S}\mathbf{p}\|_2^2 \quad (16)$$

and

$$\Psi_2(\mathbf{p}) = \|\mathbf{T}\mathbf{p}\|_2^2, \quad (17)$$

where  $\mathbf{S}$  and  $\mathbf{T}$  are matrices given by:

$$\mathbf{S} = \begin{bmatrix} \mathbf{R} & \mathbf{0} & \mathbf{0} \end{bmatrix}_{(N-1) \times M} \quad (18)$$

and

$$\mathbf{T} = \begin{bmatrix} \mathbf{0} & \mathbf{R} & \mathbf{0} \end{bmatrix}_{(N-1) \times M}. \quad (19)$$

In these equations,  $\mathbf{R}$  is defined by equation 14 and  $\mathbf{0}$  are matrices with all elements equal to zero.

## Equality constraints

In order to incorporate a priori information at isolated points on the basement and Moho surfaces, we use an approach similar to those proposed by Barbosa et al. (1997) and Barbosa et al. (1999a).

### *Equality constraint on vector $\mathbf{t}^{(Q)}$*

Let  $\mathbf{a}$  be a vector whose  $k$ -th element  $a_k$ ,  $k = 1, \dots, A$ , is the difference between a known basement depth and the sum of the thickness of the upper parts of the interpretation model (water layer and the upper sub-layers of Layer 2), all at the same horizontal coordinate  $y_k^A$  of the profile. These differences, which must be positive, are used to define the regularizing

function  $\Psi_2(\mathbf{p})$  (equation 3):

$$\Psi_2(\mathbf{p}) = \|\mathbf{A}\mathbf{p} - \mathbf{a}\|_2^2, \quad (20)$$

where  $\mathbf{A}$  is an  $A \times M$  matrix whose  $k$ -th line has one element equal to one and all the remaining elements equal to zero. The location of the single non-null element in the  $k$ -th line of  $\mathbf{A}$  depends on the coordinate  $y_k^A$  of the known thickness  $a_k$ . Let us consider, for example, an interpretation model formed by  $N = 10$  columns. Consider also that the thickness of the deepest sub-layer of Layer 2 at the coordinates  $y_1^A = y_4$  and  $y_2^A = y_9$  are equal to 25 and 35.7 km, respectively. In this case,  $A = 2$ ,  $\mathbf{a}$  is a  $2 \times 1$  vector with elements  $a_1 = 25$  and  $a_2 = 35.7$  and  $\mathbf{A}$  is a  $2 \times M$  matrix ( $M = 2N + 1 = 21$ ). The element 4 of the first line and the element 9 of the second line of  $\mathbf{A}$  are equal to 1 and all its remaining elements are equal to zero.

*Equality constraint on vector  $\mathbf{t}^{(m)}$*

Let  $\mathbf{b}$  be a vector whose  $k$ -th element  $b_k$ ,  $k = 1, \dots, B$ , is the difference between the compensation depth  $S_0$  and the known Moho depth at the horizontal coordinate  $y_k^B$  of the profile. These differences, which must be positive, define known thickness values of the upper part of Layer 4. These values are used to define the regularizing function  $\Psi_3(\mathbf{p})$  (equation 3):

$$\Psi_3(\mathbf{p}) = \|\mathbf{B}\mathbf{p} - \mathbf{b}\|_2^2, \quad (21)$$

where  $\mathbf{B}$  is a  $B \times M$  matrix whose  $k$ -th line has one element equal to one and all the remaining elements equal to zero. This matrix is defined in the same way as matrix  $\mathbf{A}$  (equation 20).



## Computational procedures for solving of the inverse problem

The parameter vector  $\mathbf{p}$  (equation 1) minimizing the goal function  $\Gamma(\mathbf{p})$  (equation 3), subjected to the inequality constraint (equation 4), is estimated in three steps (Step 1, Step 2 and Step 3 described in the following subsections). At each step, the goal function is minimized by using the Levenberg-Marquardt method (Silva et al., 2001; Aster et al., 2005) and the inequality constraint (equation 4) is incorporated by using the same strategy employed by Barbosa et al. (1999b). All derivatives of the misfit function  $\Phi(\mathbf{p})$  (equation 5) with respect to the parameters are computed by using a finite difference approximation.

### *Considerations about the weights $\mu_0, \mu_1, \mu_2, \mu_3$ and $\mu_4$*

An important aspect of our method is related to the values attributed to the weights  $\mu_\ell$  (equation 3). Their values can be very dependent on the particular characteristics of the interpretation model and there is no analytical rule to define them. To overcome this problem, we normalize the  $\mu_\ell$  values as follows:

$$\mu_\ell = \tilde{\mu}_\ell \frac{E_\Phi}{E_\ell}, \quad \ell = 0, \dots, 4, \quad (22)$$

where  $\tilde{\mu}_\ell$  is a positive scalar and  $E_\Phi/E_\ell$  is a normalizing constant. In this equation,  $E_\ell$  represents the median of the elements forming the main diagonal of the Hessian matrix of the  $\ell$ -th constraining function  $\Psi_\ell(\mathbf{p})$  (equations 15, 16, 17, 20 and 21). The constant  $E_\Phi$  is defined in a similar way by using the Hessian matrix of the misfit function  $\Phi(\mathbf{p})$  (equation 5) computed with the initial approximation  $\mathbf{p}^{(0)}$  for the parameter vector  $\mathbf{p}$  (equation 1) at the Step 1 (described in the following subsection). According to this empirical strategy, the weights  $\mu_\ell$  are defined by using the positive scalars  $\tilde{\mu}_\ell$  (equation 22), which are less dependent on the particular characteristics of the interpretation model.

### Step 1

This step is represented in blue at the flow diagram shown in Figure 3. It consists in solving the inverse problem without imposing the isostatic constraint, by using  $\tilde{\mu}_0 = 0$  (equation 22). At this step, the interpreter must set:

- Parameters defining the interpretation model (Figure 2): density contrasts  $\Delta\rho^{(\alpha)}$ ,  $\alpha = w, 1, \dots, Q, cc, oc, m$ , COT position  $y_{COT}$ , thickness  $t_i^{(w)}$  of the prisms defining Layer 1, thickness  $t_i^{(q)}$ ,  $i = 1 \dots, N$ , of the prisms forming the upper  $Q - 1$  sub-layers of Layer 2 and isostatic compensation depth  $S_0$ . Figure 2 illustrates the case in which the second layer is formed by  $Q = 2$  parts. This number, however, can be changed according to the study area.
- Parameters for the inversion: weights  $\tilde{\mu}_\ell$ ,  $\ell = 1, \dots, 4$  (equation 22), associated to the smoothness and equality constraints (equations 16, 17, 20 and 21), lower and upper bounds  $p_j^{min}$  and  $p_j^{max}$  (equation 4),  $j = 1, \dots, M$ , for the parameters to be estimated, vectors **a** (equation 20) and **b** (equation 21) containing known thickness values and an initial approximation  $\mathbf{p}^{(0)}$  for the parameter vector **p** (equation 1). The initial approximation  $\mathbf{p}^{(0)}$  must satisfy the inequality constraints (equation 4).

The initial approximation  $\mathbf{p}^{(0)}$  is used to compute the Hessian matrix of the misfit function  $\Phi(\mathbf{p})$  (equation 5), which is subsequently used to compute the constant  $E_\Phi$  (equation 22). The estimated parameter vector obtained at the end of Step 1 is conveniently called  $\mathbf{p}^{(1)}$ . The main goal in this step is finding suitable values for the parameters defining the interpretation model and those used for inversion. Several trials may be necessary to find suitable values for these parameters.

### *Step 2*

Step 2 is represented in red at the flow diagram (Figure 3) and consists in obtaining an estimated parameter vector  $\mathbf{p}^{(2)}$  by imposing full isostatic equilibrium on the interpretation model along the entire profile. In this step, the interpreter must use the same initial approximation  $\mathbf{p}^{(0)}$  of Step 1. Additionally, the interpreter must set the matrix  $\mathbf{W}$  equal to the identity and find a suitable value for the weight  $\tilde{\mu}_0$  (equation 22) controlling the isostatic constraint (equation 15). We presume that, by imposing full isostatic equilibrium along the entire profile, the estimated parameter vector  $\mathbf{p}^{(2)}$  will produce a mostly good data fit, except at some isolated regions. We assume that, at these regions, the passive margin deviates from the local isostatic equilibrium.

### *Step 3*

Step 3 represented in green at the flow diagram (Figure 3). It consists in using  $\mathbf{p}^{(2)}$  as initial approximation to obtain an estimated parameter vector  $\mathbf{p}^{(3)}$  by imposing different amounts of isostatic equilibrium on the interpretation model along the profile. At this step, the interpreter must compute the diagonal elements  $w_{ii}$  of the matrix  $\mathbf{W}$  (equation 15) in order to enable the interpretation model to deviate from isostatic equilibrium in the regions presenting large residuals. The elements of  $\mathbf{W}$  are computed as follows:

$$w_{ii} = \exp \left[ -\frac{\left( r_i^{(2)} + r_{i+1}^{(2)} \right)^2}{4\sigma} \right], \quad (23)$$

where  $\sigma$  is a positive constant,  $\mathbf{p}^{(2)}$  is the estimated parameter vector obtained in the previous step and the variables  $r_i^{(2)} = d_i^o - d_i(\mathbf{p}^{(2)})$  and  $r_{i+1}^{(2)} = d_{i+1}^o - d_{i+1}(\mathbf{p}^{(2)})$  represent, respectively, the residuals between observed and predicted data (equation 2) at the positions  $(x_i, y_i, z_i)$  and  $(x_{i+1}, y_{i+1}, z_{i+1})$ . Notice that equation 23 defines elements  $w_{ii}$  in the interval

$]0, 1]$ . Additionally, this equation results in  $w_{ii} \approx 1$  at regions where the residuals are close to zero and  $w_{ii} \approx 0$  at regions presenting large residuals. The positive constant  $\sigma$  controls the deviation from isostatic equilibrium. Small  $\sigma$  values allow large deviations from isostatic equilibrium, resulting in estimated models close to that obtained at Step 1. Large  $\sigma$  values allow small deviations from isostatic equilibrium, resulting in estimated models close to that obtained at Step 2. This strategy to define the elements of matrix  $\mathbf{W}$  (equation 15) presumes that the isostatic constraint may produce large residuals at some regions along the profile. To counteract this problem, our method enables the interpretation model to deviate from isostatic equilibrium at these regions. This idea is in agreement with the fact that isostatic equilibrium at passive rifted margin cannot be totally explained by local models.

### *Practical considerations*

Our algorithm depends on several parameters that significantly impact the estimated models and cannot be automatically set without the interpreters judgment. They are the parameters  $\tilde{\mu}_1$ ,  $\tilde{\mu}_2$ ,  $\tilde{\mu}_3$  and  $\tilde{\mu}_4$  (Step 1),  $\tilde{\mu}_0$  (Step 2) and  $\sigma$  (Step 3). Based on our practical experience, we suggest some empirical procedures for setting these parameters at each step. They are schematically represented at the flow diagram (Figure 3).

At Step 1, set  $\tilde{\mu}_1 = \tilde{\mu}_2 = 0$  and try different positive values for  $\tilde{\mu}_3$  and  $\tilde{\mu}_4$ . These two parameters control the equality constraints (equations 20 and 21) imposing a priori information at isolated points on the basement and Moho surfaces. Good guesses are, respectively,  $10^1$  and  $10^2$ . Normally,  $\tilde{\mu}_4$  is one order of magnitude greater than  $\tilde{\mu}_3$ . The parameters  $\tilde{\mu}_3$  and  $\tilde{\mu}_4$  must be the smallest positive numbers resulting in an estimated model  $\mathbf{p}'$  with basement and Moho surfaces close to the values provided by the a priori

information at some isolated points. Notice that  $\mathbf{p}'$  is an intermediate model obtained by using only the equality constraints. Consequently, there must be some pinnacles in the estimated models, around the points associated with the a priori information. This effect has already been observed by Barbosa et al. (1997). The acceptability criterion described above to define the values of  $\tilde{\mu}_3$  and  $\tilde{\mu}_4$  is represented by the decision point  $D(\tilde{\mu}_3, \tilde{\mu}_4)$  at the flow diagram (Figure 3).

By using the chosen values for  $\tilde{\mu}_3$  and  $\tilde{\mu}_4$ , try different positive values for  $\tilde{\mu}_1$  and  $\tilde{\mu}_2$ . These parameters control the smoothness of basement and Moho surfaces (equations 16 and 17). Usually,  $\tilde{\mu}_2$  is one order of magnitude greater than  $\tilde{\mu}_1$ . Good guesses are  $10^1$  and  $10^2$ . These parameters must be the smallest positive numbers producing an estimated model satisfying the following conditions: (i) the data fit must be good along the entire profile and (ii) the pinnacles must be completely removed or attenuated as much as possible. This acceptability criterion to define the values of  $\tilde{\mu}_1$  and  $\tilde{\mu}_2$  is represented by the decision point  $D(\tilde{\mu}_1, \tilde{\mu}_2)$  at the flow diagram (Figure 3).

At Step 2, try different positive values for  $\tilde{\mu}_0$  (equation 22). This parameter controls the smoothness of the lithostatic stress exerted by the interpretation model at the compensation depth  $S_0$ . Generally,  $\tilde{\mu}_0$  is one or two orders of magnitude greater than  $\tilde{\mu}_1$ . Good guesses are  $10^2$  or  $10^3$ . Large values produce a poor data fit along the profile. This parameter must be the largest positive number resulting in an estimated model satisfying two conditions: (i) the lithostatic stress curve must be smooth along the entire profile and (ii) there must be a good data fit along the entire profile, except at some isolated regions that can show relatively large residuals. This acceptability criterion for the value of  $\tilde{\mu}_0$  is represented by the decision point  $D(\tilde{\mu}_0)$  at the flow diagram (Figure 3).

Finally, at Step 3, try different positive values for  $\sigma$  (equation 23). This parameter controls the deviations of the interpretation model from the isostatic equilibrium at regions presenting large residuals. Small values produce estimated models close to that obtained at Step 1. On the other hand, large values produce estimated models close to that obtained at Step 2. This parameter must be set as the largest positive number producing (i) a good data-fit along the entire profile and (ii) an estimated model different from those obtained at Steps 1 and 2. This acceptability criterion to define the value of  $\sigma$  is represented by the decision point  $D(\sigma)$  at the flow diagram (Figure 3). A good practice is to generate a set of estimates by using different values for  $\sigma$ .

## APPLICATIONS TO SYNTHETIC DATA

We have simulated a simple continental margin formed by four layers: water, sediments, crust (continental and oceanic) and mantle. This model is based on a seismic profile crossing the East Greenland margin, over the Jameson Land basin (Peron-Pinvidic et al., 2013), and shows an extreme crustal thinning. Parameters defining this model are shown in Table 1. The density values of our model are compatible with those commonly used in literature (e.g., Gradmann et al., 2017). By following the algorithm described in the previous section, we inverted the simulated gravity disturbance produced by our synthetic margin.

Figure 4 shows the intermediate model  $\mathbf{p}'$  obtained at Step 1 (Figure 3) by using only the equality constraints with parameters  $\tilde{\mu}_3 = 10^1$  and  $\tilde{\mu}_4 = 10^2$ . The remaining parameters  $\tilde{\mu}_0$ ,  $\tilde{\mu}_1$  and  $\tilde{\mu}_2$  are equal to zero. The interpretation model was defined by using the parameters shown in Table 1. We assumed  $S_0 = 48$  km and chose an initial approximation for  $\Delta S$  equal to 7 km, which corresponds to a reference Moho deeper than the true one (Table 1). Notice that, not only the initial approximation for the reference Moho, but also those for basement

and Moho surfaces (dashed blue lines) are very different from the true model (continuous black lines). As we can see, there are pinnacles around the a priori information at the basement and Moho. Despite the good data fit, the estimated model does not retrieve the true geometries of basement and Moho.

Figure 5 shows the estimated model  $\mathbf{p}^{(1)}$  obtained at the end of Step 1 (Figure 3) with  $\tilde{\mu}_1 = 10^1$  and  $\tilde{\mu}_2 = 10^2$ . By using these values, the method was able to remove the pinnacles observed in the intermediate model. As we can see, the estimated Moho and reference Moho are very close to the true ones. On the other hand, the estimated basement is smooth and present large differences ( $\approx 5$  km) relative to the true one at the region between 100 and 150 km, where the model shows a pronounced crustal thinning. Despite these large differences, the predicted gravity disturbance and lithostatic stress are very close to the simulated values.

Figure 6 shows the estimated model  $\mathbf{p}^{(2)}$  obtained at the end of Step 2 (Figure 3), by using  $\tilde{\mu}_0 = 10^3$  (equation 22). In comparison to the estimated model  $\mathbf{p}^{(1)}$  (Figure 5), this model shows a very smooth lithostatic stress curve as a consequence of the isostatic constraint. This constraint has produced little effect on the estimated reference Moho, resulted in a relatively worse estimated Moho and also produced large residuals at the regions close to 120 and 200 km. On the other hand, it reduced the large differences between the estimated and true basement surfaces. The main improvement occurs at the region between 100 and 150 km, where the true model exhibits a pronounced crustal thinning. Additional tests show in a supplementary material show that, by varying only the initial approximations for basement and Moho, our method produces practically the same estimated model shown in Figure 5. These additional results illustrate the robustness of our method to the initial approximations used in the non-linear inversion.

Figures 7, 8 and 9 show estimated models  $\mathbf{p}^{(3)}$  obtained at the Step 3 (Figure 3) by using different values for the parameter  $\sigma$  (equation 23). By comparing with estimated model  $\mathbf{p}^{(2)}$  (Figure 6), the new models show better data fits and improved estimates for Moho and reference Moho. The main differences are concentrated at the regions coinciding with large residuals at Figure 6. Notice that, at these regions, the new lithostatic stress curves contain abrupt variations and the estimated models deviate from the isostatic equilibrium.

The estimated model obtained with the smallest  $\sigma$  (Figure 7) is close to that obtained at Step 1 (Figure 5). In this case, the predicted lithostatic stress curve shows large variations and the estimated model is far from the isostatic equilibrium. On the other hand, the estimated model obtained with the largest  $\sigma$  (Figure 9) is close to that obtained at Step 2 (Figure 6). In this case, the predicted lithostatic stress curve is very smooth and the estimated model is close to the isostatic equilibrium. In comparison to these two models, that shown in Figure 8 exhibits an intermediate isostatic equilibrium. Despite these differences, all of them produce a very good data fit along the entire profile, as well as have estimated Moho and reference Moho very close to the true ones.

These results obtained with different  $\sigma$  values (equation 23) show that the isostatic constraint is not able to completely remove the ambiguity of the inverse problem. They show that, by properly combining all the constraints, our method is able to produce a set of estimated models exhibiting different amounts of isostatic equilibrium, but practically the same data fit. The differences are concentrated at the central part of the profile, where the true lithostatic curve contains large variations. At the extremities, these models are very similar to each other, the lithostatic curves are almost flat and the models are close to the isostatic equilibrium.



## APPLICATION TO REAL DATA

We applied our method to invert the gravity disturbance data on a profile located over the Pelotas basin (Stica et al., 2014), southern of Brazil (Figure 10). This basin is considered a classical example of volcanic margin (Geoffroy, 2005). The gravity disturbance data are provided by the combined global gravity field model EIGEN-6C4 (Förste et al., 2014), one of the latest releases of the “European Improved Gravity model of the Earth by New techniques” series. We have used data from ETOPO-1 to constraint the bathymetry along the profile (Amante and Eakins, 2009). Additionally, we have used a priori information about the basement and Moho depths obtained from the seismic interpretations presented by Stica et al. (2014) and Zalán (2015) to define the equality constraints (equations 20 and 21) and the initial approximation used in the non-linear inversion.

Figure 12 shows the estimated model obtained at Step 2. Parameters defining the interpretation model are shown in (Table 2). As we can see, the estimated model produces a good data fit along the whole profile, except at region  $\approx 150$  km. Figures 13, 14 and 15 show estimated models obtained at Step 3 by using different values for the parameter  $\sigma$  (equation 23). Differently from the model obtained at Step 2 (Figure 12), the new models show very good data fits along the entire profile. The estimated lithostatic stress curves produced by these estimated models show abrupt variations close to 150 km and are practically flat on the remaining parts of the profile. These results suggest that the margin is mostly in isostatic equilibrium, except at the region  $\approx 150$ . Figure 16 shows an alternative model obtained at Step 3. Besides the parameter  $\sigma$  (equation 23), the density values in Layer 2 (sediment + SDR) are different from those used to obtain the models shown in Figures 13, 14 and 15. The corresponding estimated model obtained at Step 1 is

not shown and that obtained at Step 2 is represented by the dashed blue lines.

The estimated models shown in Figures 14 and 16 are close to those proposed by Stica et al. (2014) and Zalán (2015) (continuous black lines). The larger differences ( $\approx 10$  km) occur at the basement, along the first 100 km of the profile. At this region, Zalán proposes a steep variation in basement relief, which shows a maximum depth  $\approx 30$  km. These differences may be associated to the data we used to obtain our model. We used satellite gravity data, whereas Stica et al. (2014) and Zalán (2015) used gravity, magnetic and seismic sections available to the petroleum industry. These differences may also be associated to lateral density variations which had not been included in our model, located in the sediment, SDR, crust or mantle. Alternatively, they might represent underplated mafic to ultra-mafic magma at the base of the crust, which would represent positive anomalous masses and produce a gravity high. In order to compensate this high, the inversion would estimate a deeper basement, which would be closer to Zalán’s model. We do not attempt to propose a new model for the Pelotas basin, but show how simple isostatic considerations can be combined with a priori information to explore the range of acceptable models.

## CONCLUSIONS

We present a new gravity method for simultaneously estimating the geometries of basement and Moho, as well as the constant depth of the reference Moho on a profile crossing a passive rifted margin. The method is formulated as a non-linear inverse problem by imposing local isostatic equilibrium. The parameters to be estimated define the geometries of basement and Moho, as well as a constant depth defining the reference Moho. There are three main differences between our method and those in the literature. The first is that, at each iteration of the non-linear inversion, our method estimates corrections for the geometries

of basement and Moho simultaneously. It means that we do not estimate the Moho, use it to compute a residual gravity anomaly and then invert these residual data to obtain the basement. Another difference is that we do not use local isostasy to directly link the geometries of basement and Moho. Rather, we impose smoothness on the lithostatic stress exerted by the interpretation model on a constant compensation depth, below which there is no lateral density variations. Finally, our method also differs from those in the literature because it attempts to use isostasy for exploring (and not necessarily reducing) the inherent ambiguity of gravity methods.

Tests with synthetic data produced by a realistic model show that our method can be used to generate a set of possible solutions that have different “degrees of isostatic equilibrium” and produced an equally good data fit. The interpreter must choose the “best estimated model” based on the available priori information and its knowledge about the study area. Besides, these results show that the isostatic constraint can considerably improve the estimated models at rifted margins showing pronounced crustal thinning. Applications to real data over the Pelotas basin, considered a classical volcanic margin at the southern of Brazil, produced results in agreement with a previous interpretation obtained independently. These results show that, combined with priori information, our method can be a useful tool for interpreting gravity data on rifted margins.

The problem of simultaneously estimating the geometries of basement and Moho surfaces is very ambiguous and some simplifications must be made. One of these simplifications consists in considering bulk density values for each column forming the continental and oceanic crusts. The interpreter must predefine the function describing the horizontal density variation of the crust along the profile, including the region close the COT. In most practical situations, however, the interpreter will not have access to a detailed description

of the density variations within the crust and a regional approximation will have to be used instead. As a consequence, local errors in the estimated basement and Moho surfaces are expected at regions presenting local density variations in the deeper parts of continental crust and in the oceanic crust. Another limitation of our method is that it requires a priori information about the upper layers located below the water layer. This information can be obtained, for example, from seismic data and be used to set the densities of the layers located right below the ocean bottom. If no a priori information is available at the study area, the interpreter will have to use approximated values and test different models. Errors in this approximation may negatively impact the estimated model, especially in the basement surface. Further research could be conducted to generalize our method to estimate three dimensional models, include lateral density variations in the upper mantle and depth-dependent density distributions at the layers representing sediments.

## **ACKNOWLEDGMENTS**

## REFERENCES

- Amante, C., and B. Eakins, 2009, Etopo1 1 arc-minute global relief model: Procedures, data sources and analysis.
- Aster, R. C., B. Borchers, and C. H. Thurber, 2005, Parameter estimation and inverse problems (international geophysics): Academic Press.
- Bagherbandi, M., and M. Eshagh, 2012, Crustal thickness recovery using an isostatic model and goce data: *Earth, Planets and Space*, **64**, 1053–1057.
- Barbosa, V. C. F., J. ao B. C. Silva, and W. E. Medeiros, 1997, Gravity inversion of basement relief using approximate equality constraints on depths: *Geophysics*, **62**, 1745–1757.
- Barbosa, V. C. F., J. B. C. Silva, and W. E. Medeiros, 1999a, Gravity inversion of a discontinuous relief stabilized by weighted smoothness constraints on depth: *GEOPHYSICS*, **64**, 1429–1437.
- , 1999b, Stable inversion of gravity anomalies of sedimentary basins with nonsmooth basement reliefs and arbitrary density contrast variations: *GEOPHYSICS*, **64**, 754–764.
- Barnes, G., and J. Barraud, 2012, Imaging geologic surfaces by inverting gravity gradient data with depth horizons: *Geophysics*, **77**, G1–G11.
- Barzaghi, R., and L. Biagi, 2014, The collocation approach to Moho estimate: *Annals of Geophysics*.
- Bott, M. H. P., 1960, The use of rapid digital computing methods for direct gravity interpretation of sedimentary basins: *Geophysical Journal International*, **3**, 63–67.
- Braitenberg, C., E. Pagot, Y. Wang, and J. Fang, 2003, Bathymetry and crustal thickness variations from gravity inversion and flexural isostasy: *Satellite Altimetry for Geodesy, Geophysics and Oceanography*, Springer Berlin Heidelberg, 143–149.
- Braitenberg, C., F. Pettenati, and M. Zadro, 1997, Spectral and classical methods in the

- evaluation of moho undulations from gravity data: The ne italian alps and isostasy: Journal of Geodynamics, **23**, 5 – 22.
- Braitenberg, C., and M. Zadro, 1999, Iterative 3d gravity inversion with integration of seismologic data: Bollettino di Geofisica Teorica ed Applicata, **40**, 469–475.
- Camacho, A. G., J. Fernndez, and J. Gottsmann, 2011, A new gravity inversion method for multiple subhorizontal discontinuity interfaces and shallow basins: Journal of Geophysical Research: Solid Earth, **116**.
- Chakravarthi, V., and N. Sundararajan, 2007, 3d gravity inversion of basement relief a depth-dependent density approach: GEOPHYSICS, **72**, I23–I32.
- Condi, F. J., C. A. Zelt, D. S. Sawyer, and G. J. Hirasaki, 1999, Gravity inversion for rifted margin deep structure using extension and isostatic constraints: Geophysical Journal International, **138**, 435–446.
- Cordell, L., and R. G. Henderson, 1968, Iterative three-dimensional solution of gravity anomaly data using a digital computer: GEOPHYSICS, **33**, 596–601.
- Fairhead, J. D., C. M. Green, and D. Blitzkow, 2003, The use of gps in gravity surveys: The Leading Edge, **22**, 954–959.
- Ferderer, R., J. Mariano, and J. Shoffner, 2017, Inversion of gravity data using general local isostasy: 87th Annual International Meeting, SEG, Expanded Abstracts, 1718–1722.
- Förste, C., S. Bruinsma, O. Abrikosov, J.-M. Lemoine, J. C. Marty, F. Flechtner, G. Balmino, F. Barthelmes, and R. Biancale, 2014, EIGEN-6C4 The latest combined global gravity field model including GOCE data up to degree and order 2190 of GFZ Potsdam and GRGS Toulouse: <https://doi.org/10.5880/icgem.2015.1>.
- García-Abdeslem, J., 2017, Nonlinear inversion of isostatic residual gravity data from montage basin, northern gulf of california: GEOPHYSICS, **82**, G45–G55.

- Geoffroy, L., 2005, Volcanic passive margins: *Comptes Rendus Geoscience*, **337**, 1395 – 1408.
- Gradmann, S., C. Haase, and J. Ebbing, 2017, Isostasy as a tool to validate interpretations of regional geophysical datasets – application to the mid-norwegian continental margin: Geological Society, London, Special Publications, **447**, 279–297.
- Granser, H., 1987, Three-dimensional interpretation of gravity data from sedimentary basins using an exponential density-depth function: *Geophysical Prospecting*, **35**, 1030–1041.
- Guspi, F., 1993, Noniterative nonlinear gravity inversion: *Geophysics*, **58**, 935–940.
- Hackney, R. I., and W. E. Featherstone, 2003, Geodetic versus geophysical perspectives of the gravity anomaly: *Geophysical Journal International*, **154**, 35–43.
- Heiskanen, W. A., and H. Moritz, 1967, *Physical geodesy*: W.H. Freeman and Company.
- Hinze, W. J., C. Aiken, J. Brozena, B. Coakley, D. Dater, G. Flanagan, R. Forsberg, T. Hildenbrand, G. R. Keller, J. Kellogg, R. Kucks, X. Li, A. Mainville, R. Morin, M. Pilkington, D. Plouff, D. Ravat, D. Roman, J. Urrutia-Fucugauchi, M. Véronneau, M. Webring, and D. Winester, 2005, New standards for reducing gravity data: The north american gravity database: *Geophysics*, **70**, J25–J32.
- Li, X., and H.-J. Götze, 2001, Ellipsoid, geoid, gravity, geodesy, and geophysics: *Geophysics*, **66**, 1660–1668.
- Lima, W. A., C. M. Martins, J. B. Silva, and V. C. Barbosa, 2011, Total variation regularization for depth-to-basement estimate: Part 2 physicogeologic meaning and comparisons with previous inversion methods: *Geophysics*, **76**, I13–I20.
- Martins, C. M., V. C. Barbosa, and J. B. Silva, 2010, Simultaneous 3d depth-to-basement and density-contrast estimates using gravity data and depth control at few points: *GEOPHYSICS*, **75**, I21–I28.

- Martins, C. M., W. A. Lima, V. C. Barbosa, and J. B. Silva, 2011, Total variation regularization for depth-to-basement estimate: Part 1 - mathematical details and applications: *Geophysics*, **76**, I1–I12.
- Nagy, D., G. Papp, and J. Benedek, 2000, The gravitational potential and its derivatives for the prism: *Journal of Geodesy*, **74**, 311–326.
- Oldenburg, D. W., 1974, The inversion and interpretation of gravity anomalies: *Geophysics*, **39**, 526–536.
- Peron-Pinvidic, G., G. Manatschal, and P. T. Osmundsen, 2013, Structural comparison of archetypal atlantic rifted margins: A review of observations and concepts: *Marine and Petroleum Geology*, **43**, 21 – 47.
- Reamer, S. K., and J. F. Ferguson, 1989, Regularized twodimensional fourier gravity inversion method with application to the silent canyon caldera, nevada: *Geophysics*, **54**, 486–496.
- Roy, A., 1962, Ambiguity in geophysical interpretation: *Geophysics*, **27**, 90–99.
- Salem, A., 2017, Gravity modeling a rifted continental margin.
- Salem, A., C. Green, M. Stewart, and D. D. Lerma, 2014, Inversion of gravity data with isostatic constraints: *GEOPHYSICS*, **79**, A45–A50.
- Sampietro, D., 2015, Geological units and moho depth determination in the western balkans exploiting goce data: *Geophysical Journal International*, **202**, 1054–1063.
- Sen, M. K., and P. L. Stoffa, 2013, Global optimization methods in geophysical inversion, second edition ed.: Cambridge University Press.
- Shin, Y. H., C.-K. Shum, C. Braitenberg, S. M. Lee, H. Xu, K. S. Choi, J. H. Baek, and J. U. Park, 2009, Three-dimensional fold structure of the tibetan moho from grace gravity data: *Geophysical Research Letters*, **36**.



- Silva, J. B., D. C. Costa, and V. C. Barbosa, 2006, Gravity inversion of basement relief and estimation of density contrast variation with depth: *GEOPHYSICS*, **71**, J51–J58.
- Silva, J. B., A. S. Oliveira, and V. C. Barbosa, 2010, Gravity inversion of 2d basement relief using entropic regularization: *Geophysics*, **75**, I29–I35.
- Silva, J. B. C., W. E. Medeiros, and V. C. F. Barbosa, 2001, Pitfalls in nonlinear inversion: pure and applied geophysics, **158**, 945–964.
- Silva, J. B. C., and D. F. Santos, 2017, Efficient gravity inversion of basement relief using a versatile modeling algorithm: *GEOPHYSICS*, **82**, G23–G34.
- Silva, J. B. C., D. F. Santos, and K. P. Gomes, 2014, Fast gravity inversion of basement relief: *Geophysics*, **79**, G79–G91.
- Skeels, D. C., 1947, Ambiguity in gravity interpretation: *Geophysics*, **12**, 43–56.
- Stewart, J., A. B. Watts, and J. G. Bagguley, 2000, Three-dimensional subsidence analysis and gravity modelling of the continental margin offshore Namibia: *Geophysical Journal International*, **141**, 724–746.
- Stica, J. M., P. V. Zalán, and A. L. Ferrari, 2014, The evolution of rifting on the volcanic margin of the pelotas basin and the contextualization of the paranetendeka lip in the separation of gondwana in the south atlantic: *Marine and Petroleum Geology*, **50**, 1 – 21.
- Tanner, J. G., 1967, An automated method of gravity interpretation: *Geophysical Journal of the Royal Astronomical Society*, **13**, 339–347.
- Turcotte, D. L., and G. Schubert, 2002, *Geodynamics*, 2 ed.: Cambridge Univ. Press.
- Uieda, L., and V. C. Barbosa, 2017, Fast nonlinear gravity inversion in spherical coordinates with application to the south american moho: *Geophysical Journal International*, **208**, 162–176.

- Uieda, L., V. C. Oliveira Jr., and V. C. F. Barbosa, 2013, Modeling the earth with fatiando a terra: Proceedings of the 12th Python in Science Conference, 96 – 103.
- Vajda, P., P. Vaníček, and B. Meurers, 2006, A new physical foundation for anomalous gravity: *Studia Geophysica et Geodaetica*, **50**, 189–216.
- Vajda, P., P. Vaníček, P. Novák, R. Tenzer, and A. Ellmann, 2007, Secondary indirect effects in gravity anomaly data inversion or interpretation: *Journal of Geophysical Research: Solid Earth*, **112**.
- van der Meijde, M., J. Julià, and M. Assumpção, 2013, Gravity derived moho for south america: *Tectonophysics*, **609**, 456 – 467. (Moho: 100 years after Andrija Mohorovicic).
- Zalán, P. V., 2015, Similarities and differences between magma-poor and volcanic passive margins applications to the brazilian marginal basins: 14th International Congress of the Brazilian Geophysical Society & EXPOGEF, Rio de Janeiro, Brazil, 3-6 August 2015, 37–42.

## LIST OF TABLES

1 Properties of the synthetic margin model. The model extends from  $y = 0$  km to  $y = 380$  km, the Continent-Ocean Transition (COT) is located at  $y_{COT} = 165$  km and the reference Moho is located at 53 km (Figures 1 and 2). The density contrasts  $\Delta\rho^{(\alpha)} = \rho^{(\alpha)} - \rho^{(r)}$  were defined by using the reference value  $\rho^{(r)} = 2850$  kg/m<sup>3</sup>, which coincides with the density  $\rho^{(cc)}$  attributed to the continental crust.

2 Properties used in the Pelotas volcanic margin. The interpretation model extends from  $y = 0$  km to  $y = 383$  km, the Continent-Ocean Transition (COT) is located at  $y_{COT} = 350$  km and the reference Moho is located at 43 200 km (Figures 1 and 2). The density contrasts  $\Delta\rho^{(\alpha)} = \rho^{(\alpha)} - \rho^{(r)}$  were defined by using the reference value  $\rho^{(r)} = 2870$  kg/m<sup>3</sup>, which coincides with the density  $\rho^{(cc)}$  attributed to the continental crust.

## LIST OF FIGURES

1     Rifted margin model formed by four layers. Layer 1 represents a water with constant density  $\rho^{(w)}$ . Layer 2 is split into  $Q$  sub-layers according to the complexity of the study area. In this example,  $Q = 2$ . These sub-layers represent sediments, salt or volcanic rocks and have constant densities  $\rho^{(q)}$ ,  $q = 1, \dots, Q$ . Layer 3 represents the crust. In this example, its density  $\rho(c)$  assumes two possible values  $\rho^{(cc)}$  and  $\rho^{(oc)}$  representing, respectively, continental and oceanic crust. More complex models can be generated by using a function describing the lateral density variations within the crust. Finally, Layer 4 represents a homogeneous mantle with constant density  $\rho^{(m)}$ . Basement, Moho and reference Moho are represented by the dashed-white lines. The reference mass distribution is formed by an upper layer with constant density  $\rho^{(r)}$  and base at the reference Moho. Below this layer, we presume a reference distribution with the same constant density  $\rho^{(m)}$  of the mantle.

2     Interpretation model formed by  $N$  columns of vertically stacked prisms. Each column is formed by four layers of prisms and locally approximates the rifted margin model shown in Figure 1. Layer 2 is formed by  $Q$  sub-layers according to the complexity of the study area. In this example,  $Q = 2$ . The thickness  $t_i^Q$  and  $t_i^m$  of the prisms forming, respectively, the base of Layer 2 and the top of Layer 4 at the  $i$ -column are indicated. Each prism has a constant density contrast defined as the difference between its corresponding density at the rifted margin model and the constant density  $\rho^{(r)}$  of the shallowest layer forming the reference density distribution (Figure 1). Basement, Moho and the reference Moho are represented by dashed-white lines. The continuous black line represents the compensation depth at  $S_0$ . The reference Moho is located at  $S_0 + \Delta S$ .

3     Flow diagram of the algorithm. Steps 1, 2 and 3 are represented in blue, red and green, respectively. Decision points are represented by diamonds. The parallelograms

represent input parameters. The remaining processes of the algorithm are represented by rectangles. For convenience, we omitted some input parameters related to the interpretation model and the inversion (see the subsection *Step 1*). Details about this flow diagram are explained at subsection Computational procedures for solving of the inverse problem.

4 Application to synthetic data. Intermediate model  $\mathbf{p}'$  obtained at Step 1 (Figure 3) by using  $\tilde{\mu}_3 = 10^1$  and  $\tilde{\mu}_4 = 10^2$ . (Bottom panel) True and estimated surfaces, initial basement and Moho (initial guess) and a priori information at points on basement and Moho (known depths). (Middle panel) True and predicted lithostatic stress curves (equation 9). (Upper panel) Gravity disturbance produced by the true model (simulated data), estimated model (predicted data) and by the initial guess (initial guess data). The density contrasts are those shown in Table 1 and  $S_0 = 48$  km.

5 Application to synthetic data. Estimated model  $\mathbf{p}^{(1)}$  obtained at the end of Step 1 (Figure 3) by using  $\tilde{\mu}_1 = 10^1$  and  $\tilde{\mu}_2 = 10^2$ . The remaining information is the same shown in the caption of Figure 4.

6 Application to synthetic data. Estimated model  $\mathbf{p}^{(2)}$  obtained at the end of Step 2 (Figure 3) by using  $\tilde{\mu}_0 = 10^3$ . The remaining information is the same shown in the caption of Figure 4.

7 Application to synthetic data. Estimated model  $\mathbf{p}^{(3)}$  obtained at the end of Step 3 (Figure 3) by using  $\mathbf{p}^{(2)}$  (Figure 6) as initial approximation (dashed blue lines) and  $\sigma = 1$  (equation 23). The remaining information is the same shown in the caption of Figure 4.

8 Application to synthetic data. Estimated model  $\mathbf{p}^{(3)}$  obtained at the end of Step 3 (Figure 3) by using  $\mathbf{p}^{(2)}$  (Figure 6) as initial approximation (dashed blue lines) and  $\sigma = 11$  (equation 23). The remaining information is the same shown in the caption of Figure 4.

9 Application to synthetic data. Estimated model  $\mathbf{p}^{(3)}$  obtained at the end of Step 3

(Figure 3) by using  $\mathbf{p}^{(2)}$  (Figure 6) as initial approximation (dashed blue lines) and  $\sigma = 18$  (equation 23). The remaining information is the same shown in the caption of Figure 4.

10 Application to real data on Pelotas basin, Brazil. Gravity disturbance provided by the global gravity field model EIGEN-6C4 (Förste et al., 2014) at the study area. The black straight line indicates the gravity profile over the Pelotas basin. The end points of the profile have coordinates (geodetic latitude and longitude)  $(-27.72, -48.23)$  and  $(-29.66, -44.94)$ . The coordinates are referred to the WGS84 datum.

11 Application to real data on Pelotas basin, Brazil. Estimated model  $\mathbf{p}^{(1)}$  obtained at the end of Step 1 (Figure 3) by using  $\tilde{\mu}_1 = 10^1$ ,  $\tilde{\mu}_2 = 10^2$ ,  $\tilde{\mu}_3 = 10^1$  and  $\tilde{\mu}_4 = 10^2$ . (Bottom panel) Estimated surfaces, initial basement and Moho (initial guess) and a priori information at basement and Moho (known depths). The continuous black lines represent a previous interpretation presented by Zalán (2015). (Middle panel) True and predicted lithostatic stress curves (equation 9). (Upper panel) Observed gravity disturbance, data produced by the estimated model (predicted data) and data produced the by the initial approximation (initial guess data). We used  $S_0 = 41$  km, density contrasts equal to those shown in Table 2 and initial approximation for  $\Delta S$  equal to 1 km.

12 Application to real data on Pelotas basin, Brazil. Estimated model  $\mathbf{p}^{(2)}$  obtained at the end of Step 2 (Figure 3) by using  $\tilde{\mu}_0 = 10^2$ . The remaining information is the same shown in the caption of Figure 11.

13 Application to real data on Pelotas basin, Brazil. Estimated model  $\mathbf{p}^{(3)}$  obtained at the end of Step 3 (Figure 3) by using  $\mathbf{p}^{(2)}$  (Figure 12) as initial approximation (dashed blue lines) and  $\sigma = 7$  (equation 23). The remaining information is the same shown in the caption of Figure 11.

14 Application to real data on Pelotas basin, Brazil. Estimated model  $\mathbf{p}^{(3)}$  obtained

at the end of Step 3 (Figure 3) by using  $\mathbf{p}^{(2)}$  (Figure 12) as initial approximation (dashed blue lines) and  $\sigma = 17.6$  (equation 23). The remaining information is the same shown in the caption of Figure 11.

15 Application to real data on Pelotas basin, Brazil. Estimated model  $\mathbf{p}^{(3)}$  obtained at the end of Step 3 (Figure 3) by using  $\mathbf{p}^{(2)}$  (Figure 12) as initial approximation (dashed blue lines) and  $\sigma = 19$  (equation 23). The remaining information is the same shown in the caption of Figure 11.

16 Application to real data on Pelotas basin, Brazil. Alternative estimated model  $\mathbf{p}^{(3)}$  obtained at the end of Step 3 (Figure 3). The differences between this model and those shown in Figures 13, 14 and 15 are the densities  $\rho^{(1)}$  and  $\rho^{(2)}$  attributed to the sediments and SDR (Table 2), as well as the parameter  $\sigma$  (equation 23). In this alternative model,  $\rho^{(1)} = 2425 \text{ kg/m}^3$ ,  $\rho^{(2)} = 2835 \text{ kg/m}^3$  and  $\sigma = 17$ . The remaining information is the same shown in the caption of Figure 11.

<b>Geological meaning</b>	$\rho^{(\alpha)}$ (kg/m <sup>3</sup> )	$\Delta\rho^{(\alpha)}$ (kg/m <sup>3</sup> )	$\alpha$
water	1030	−1820	<i>w</i>
sediments	2600	−250	1
continental crust	2850	0	<i>cc</i>
oceanic crust	2885	35	<i>oc</i>
mantle	3250	400	<i>m</i>

Table 1: Properties of the synthetic margin model. The model extends from  $y = 0$  km to  $y = 380$  km, the Continent-Ocean Transition (COT) is located at  $y_{COT} = 165$  km and the reference Moho is located at 53 km (Figures 1 and 2). The density contrasts  $\Delta\rho^{(\alpha)} = \rho^{(\alpha)} - \rho^{(r)}$  were defined by using the reference value  $\rho^{(r)} = 2850$  kg/m<sup>3</sup>, which coincides with the density  $\rho^{(cc)}$  attributed to the continental crust.



<b>Geological meaning</b>	$\rho^{(\alpha)}$ (kg/m <sup>3</sup> )	$\Delta\rho^{(\alpha)}$ (kg/m <sup>3</sup> )	$\alpha$
water	1030	−1840	<i>w</i>
sediments	2350	−520	1
SDR	2855	−15	2
continental crust	2870	0	<i>cc</i>
oceanic crust	2885	15	<i>oc</i>
mantle	3240	370	<i>m</i>

Table 2: Properties used in the Pelotas volcanic margin. The interpretation model extends from  $y = 0$  km to  $y = 383$  km, the Continent-Ocean Transition (COT) is located at  $y_{COT} = 350$  km and the reference Moho is located at 43 200 km (Figures 1 and 2). The density contrasts  $\Delta\rho^{(\alpha)} = \rho^{(\alpha)} - \rho^{(r)}$  were defined by using the reference value  $\rho^{(r)} = 2870$  kg/m<sup>3</sup>, which coincides with the density  $\rho^{(cc)}$  attributed to the continental crust.

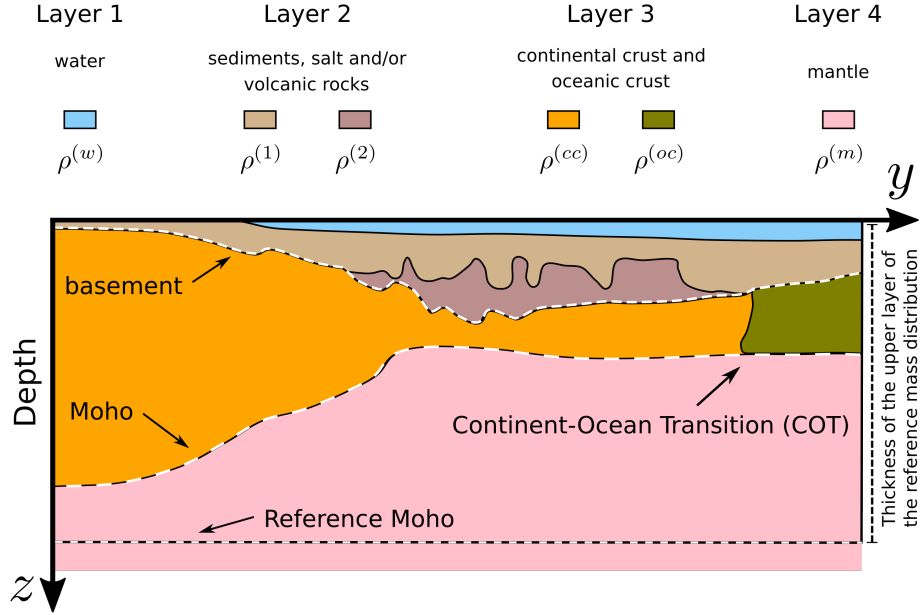


Figure 1: Rifted margin model formed by four layers. Layer 1 represents a water with constant density  $\rho^{(w)}$ . Layer 2 is split into  $Q$  sub-layers according to the complexity of the study area. In this example,  $Q = 2$ . These sub-layers represent sediments, salt or volcanic rocks and have constant densities  $\rho^{(q)}$ ,  $q = 1, \dots, Q$ . Layer 3 represents the crust. In this example, its density  $\rho(c)$  assumes two possible values  $\rho^{(cc)}$  and  $\rho^{(oc)}$  representing, respectively, continental and oceanic crust. More complex models can be generated by using a function describing the lateral density variations within the crust. Finally, Layer 4 represents a homogeneous mantle with constant density  $\rho^{(m)}$ . Basement, Moho and reference Moho are represented by the dashed-white lines. The reference mass distribution is formed by an upper layer with constant density  $\rho^{(r)}$  and base at the reference Moho. Below this layer, we presume a reference distribution with the same constant density  $\rho^{(m)}$  of the mantle.

– GEO-XXXX

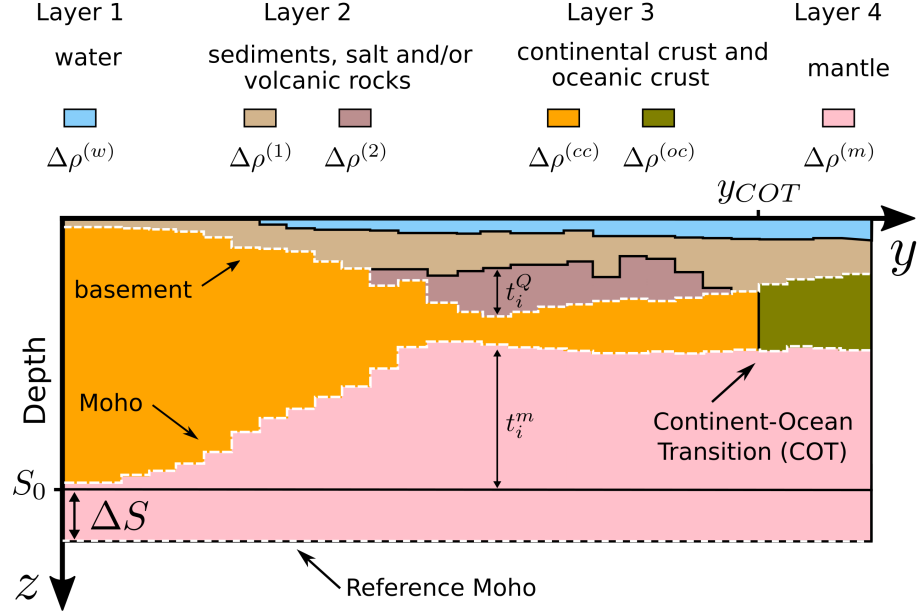


Figure 2: Interpretation model formed by  $N$  columns of vertically stacked prisms. Each column is formed by four layers of prisms and locally approximates the rifted margin model shown in Figure 1. Layer 2 is formed by  $Q$  sub-layers according to the complexity of the study area. In this example,  $Q = 2$ . The thickness  $t_i^Q$  and  $t_i^m$  of the prisms forming, respectively, the base of Layer 2 and the top of Layer 4 at the  $i$ -column are indicated. Each prism has a constant density contrast defined as the difference between its corresponding density at the rifted margin model and the constant density  $\rho^{(r)}$  of the shallowest layer forming the reference density distribution (Figure 1). Basement, Moho and the reference Moho are represented by dashed-white lines. The continuous black line represents the compensation depth at  $S_0$ . The reference Moho is located at  $S_0 + \Delta S$ .

– GEO-XXXX

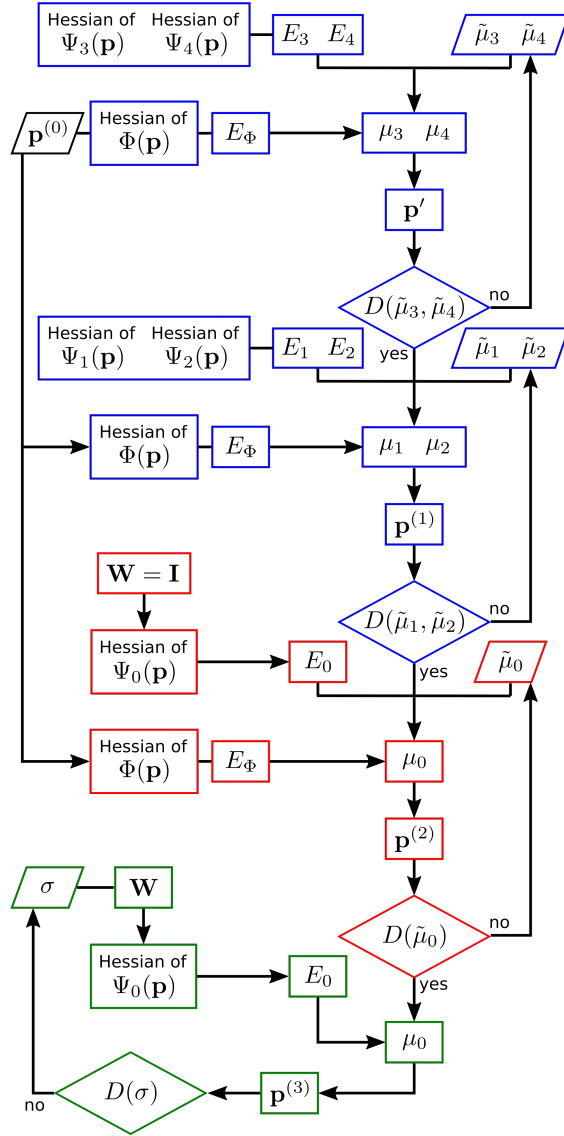


Figure 3: Flow diagram of the algorithm. Steps 1, 2 and 3 are represented in blue, red and green, respectively. Decision points are represented by diamonds. The parallelograms represent input parameters. The remaining processes of the algorithm are represented by rectangles. For convenience, we omitted some input parameters related to the interpretation model and the inversion (see the subsection *Step 1*). Details about this flow diagram are explained at subsection Computational procedures for solving of the inverse problem.

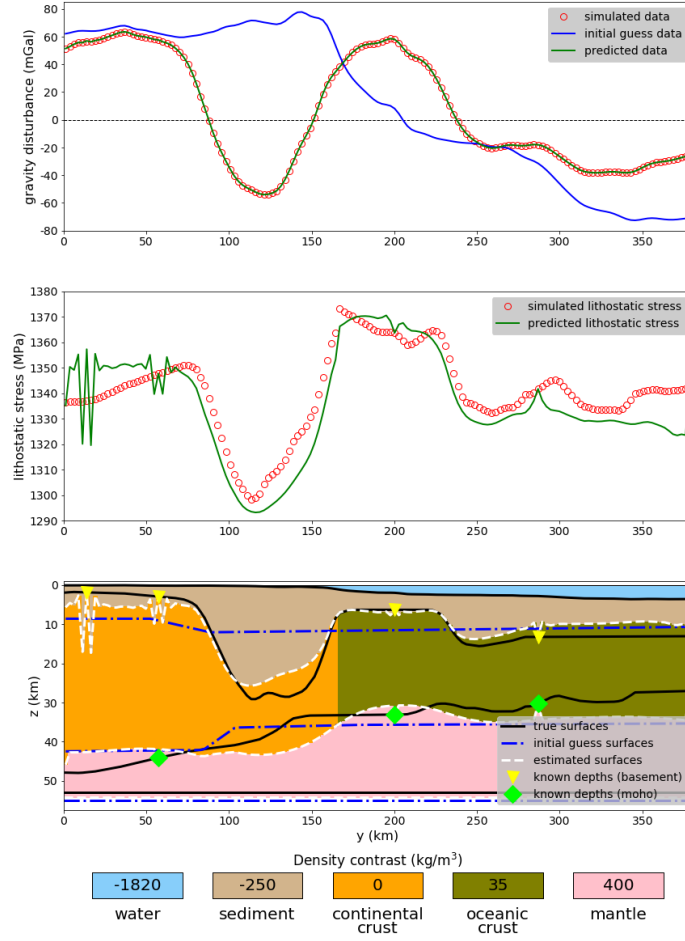


Figure 4: Application to synthetic data. Intermediate model  $\mathbf{p}'$  obtained at Step 1 (Figure 3) by using  $\tilde{\mu}_3 = 10^1$  and  $\tilde{\mu}_4 = 10^2$ . (Bottom panel) True and estimated surfaces, initial basement and Moho (initial guess) and a priori information at points on basement and Moho (known depths). (Middle panel) True and predicted lithostatic stress curves (equation 9). (Upper panel) Gravity disturbance produced by the true model (simulated data), estimated model (predicted data) and by the initial guess (initial guess data). The density contrasts are those shown in Table 1 and  $S_0 = 48$  km.

– GEO-XXXX

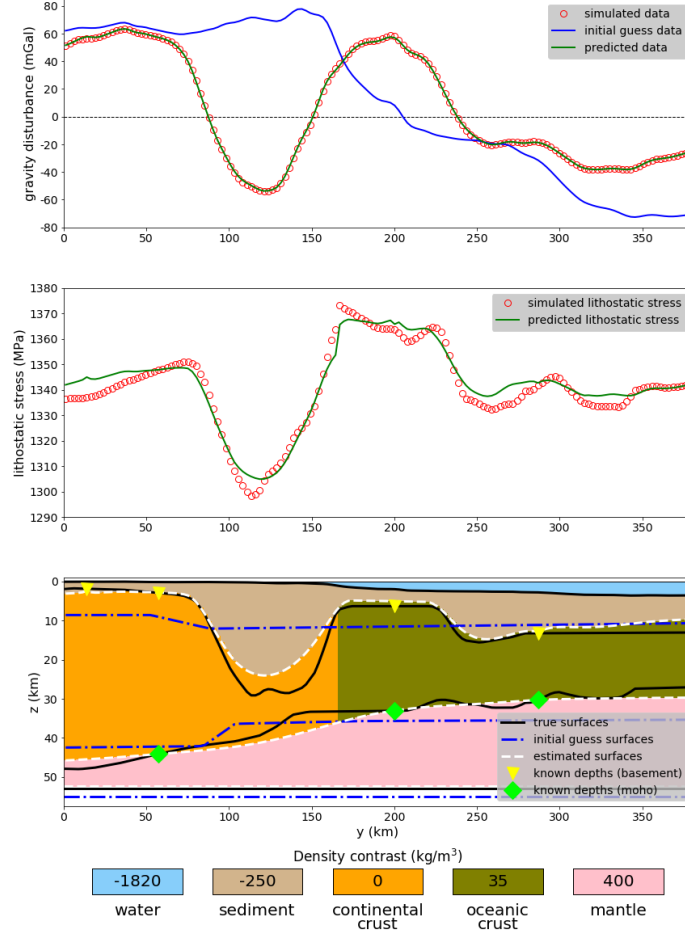


Figure 5: Application to synthetic data. Estimated model  $\mathbf{p}^{(1)}$  obtained at the end of Step 1 (Figure 3) by using  $\tilde{\mu}_1 = 10^1$  and  $\tilde{\mu}_2 = 10^2$ . The remaining information is the same shown in the caption of Figure 4.

– GEO-XXXX

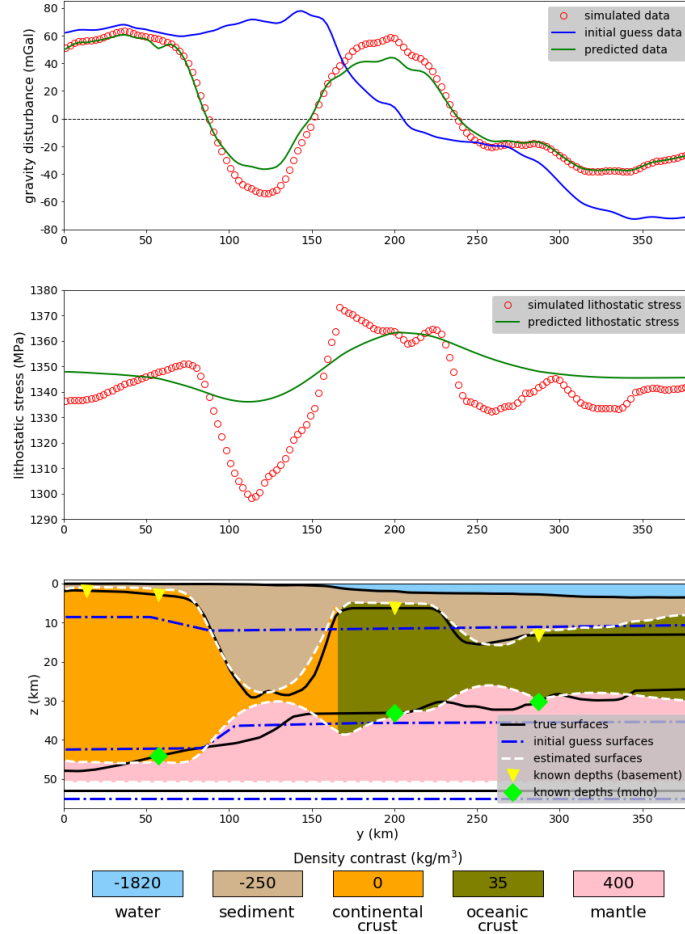


Figure 6: Application to synthetic data. Estimated model  $\mathbf{p}^{(2)}$  obtained at the end of Step 2 (Figure 3) by using  $\tilde{\mu}_0 = 10^3$ . The remaining information is the same shown in the caption of Figure 4.

– GEO-XXXX

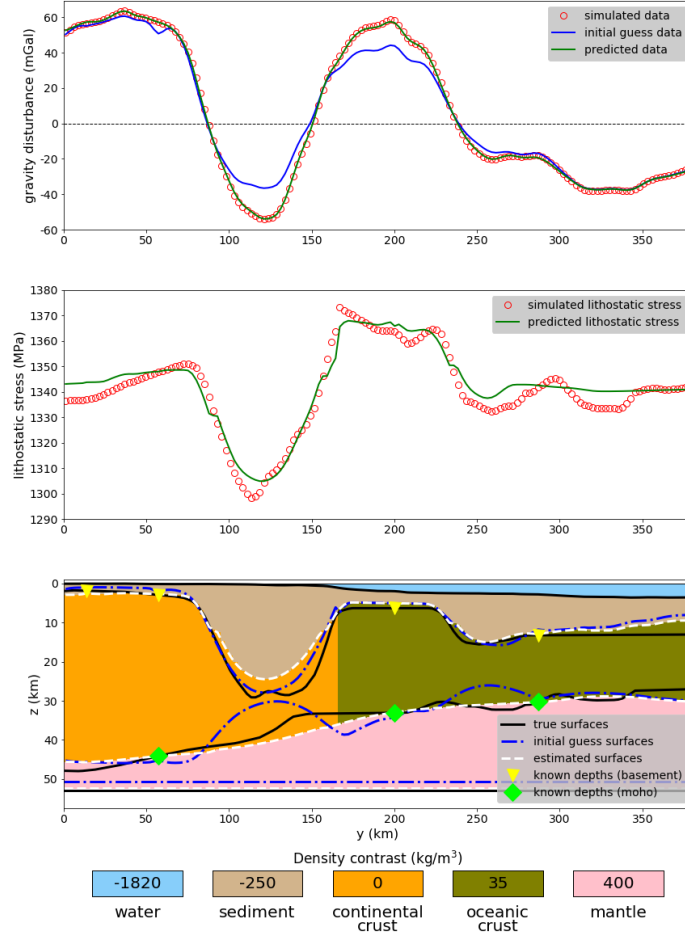


Figure 7: Application to synthetic data. Estimated model  $\mathbf{p}^{(3)}$  obtained at the end of Step 3 (Figure 3) by using  $\mathbf{p}^{(2)}$  (Figure 6) as initial approximation (dashed blue lines) and  $\sigma = 1$  (equation 23). The remaining information is the same shown in the caption of Figure 4.

– GEO-XXXX



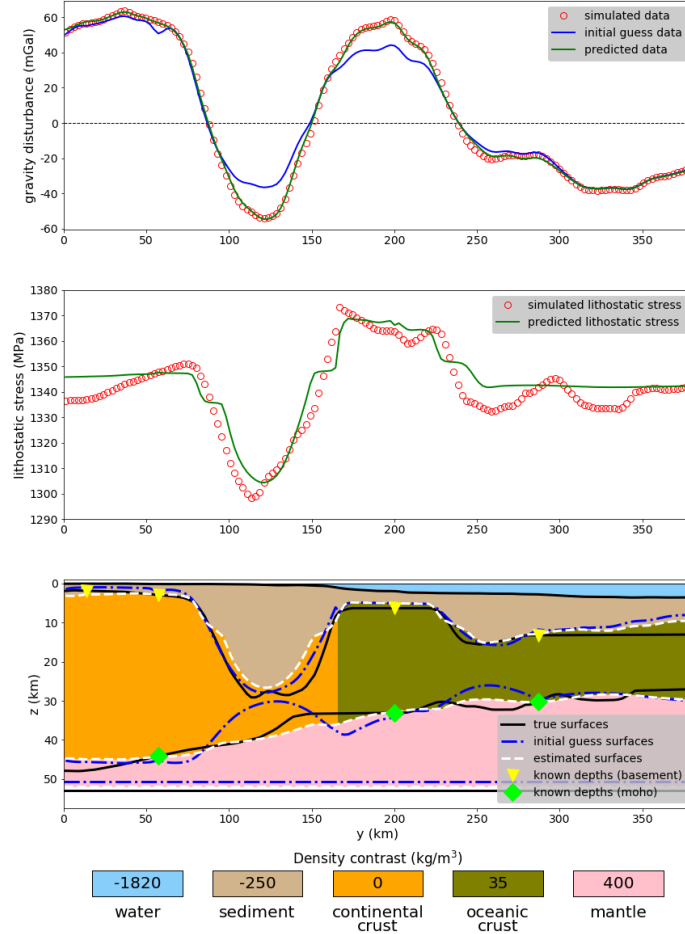


Figure 8: Application to synthetic data. Estimated model  $\mathbf{p}^{(3)}$  obtained at the end of Step 3 (Figure 3) by using  $\mathbf{p}^{(2)}$  (Figure 6) as initial approximation (dashed blue lines) and  $\sigma = 11$  (equation 23). The remaining information is the same shown in the caption of Figure 4.

– GEO-XXXX

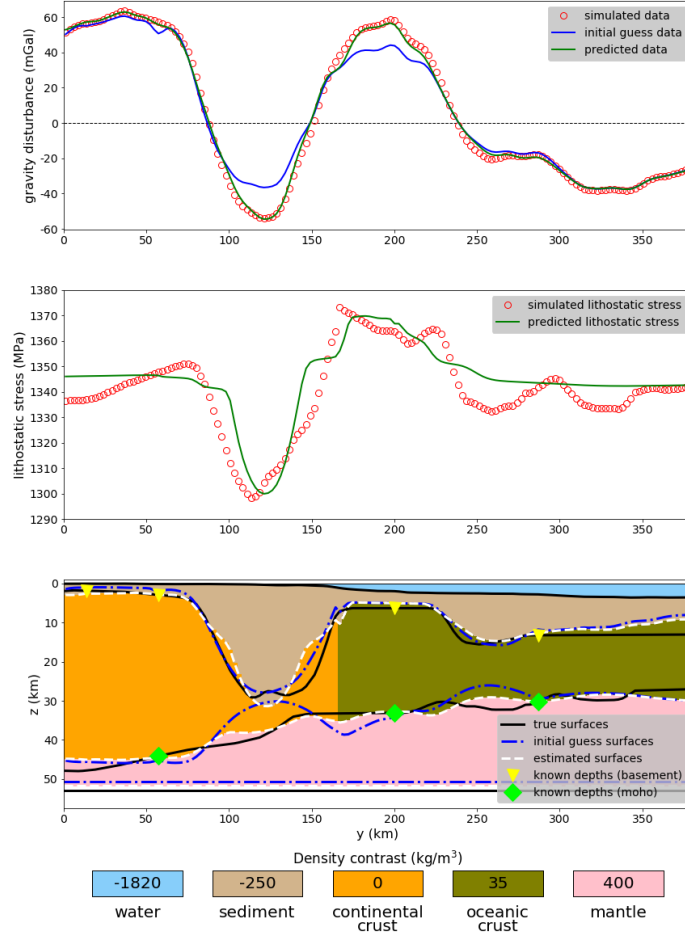


Figure 9: Application to synthetic data. Estimated model  $\mathbf{p}^{(3)}$  obtained at the end of Step 3 (Figure 3) by using  $\mathbf{p}^{(2)}$  (Figure 6) as initial approximation (dashed blue lines) and  $\sigma = 18$  (equation 23). The remaining information is the same shown in the caption of Figure 4.

– GEO-XXXX

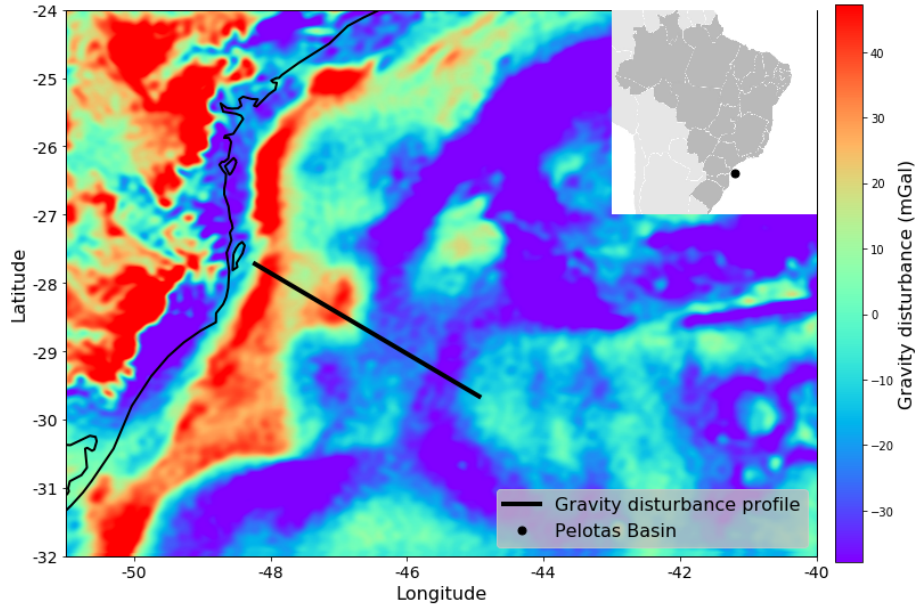


Figure 10: Application to real data on Pelotas basin, Brazil. Gravity disturbance provided by the global gravity field model EIGEN-6C4 (Förste et al., 2014) at the study area. The black straight line indicates the gravity profile over the Pelotas basin. The end points of the profile have coordinates (geodetic latitude and longitude)  $(-27.72, -48.23)$  and  $(-29.66, -44.94)$ . The coordinates are referred to the WGS84 datum.

– **GEO-XXXX**

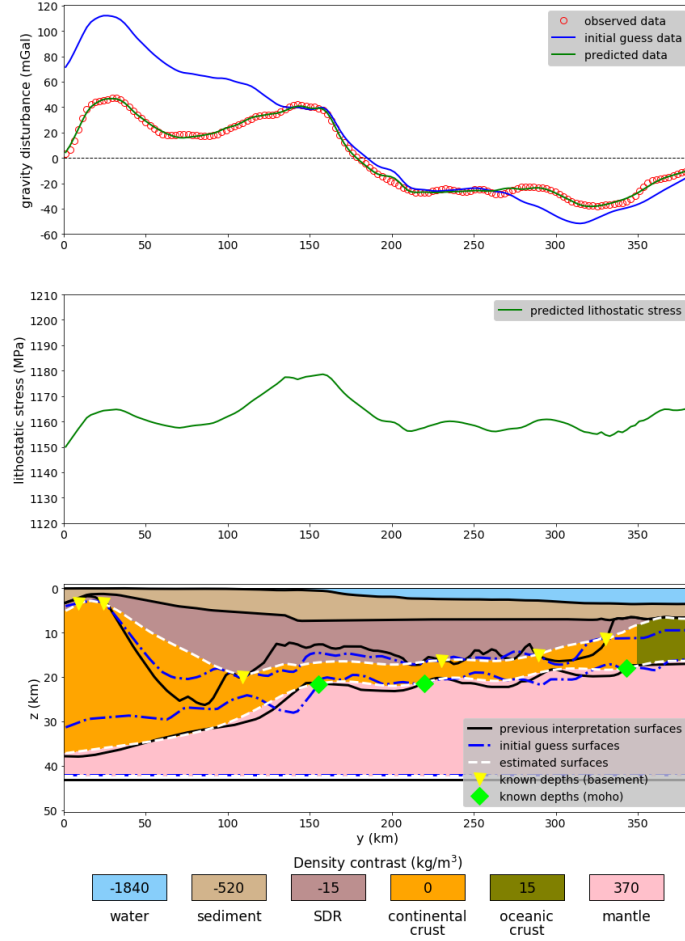


Figure 11: Application to real data on Pelotas basin, Brazil. Estimated model  $\mathbf{p}^{(1)}$  obtained at the end of Step 1 (Figure 3) by using  $\tilde{\mu}_1 = 10^1$ ,  $\tilde{\mu}_2 = 10^2$ ,  $\tilde{\mu}_3 = 10^1$  and  $\tilde{\mu}_4 = 10^2$ . (Bottom panel) Estimated surfaces, initial basement and Moho (initial guess) and a priori information at basement and Moho (known depths). The continuous black lines represent a previous interpretation presented by Zalán (2015). (Middle panel) True and predicted lithostatic stress curves (equation 9). (Upper panel) Observed gravity disturbance, data produced by the estimated model (predicted data) and data produced the by the initial approximation (initial guess data). We used  $S_0 = 41$  km, density contrasts equal to those shown in Table 2 and initial approximation for  $\Delta S$  equal to 1 km.

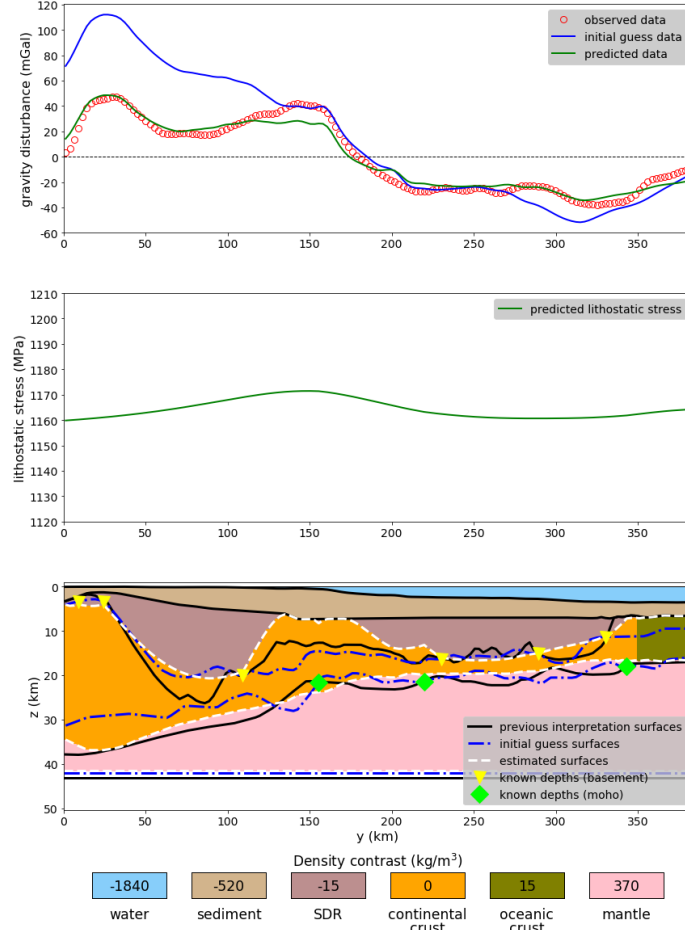


Figure 12: Application to real data on Pelotas basin, Brazil. Estimated model  $\mathbf{p}^{(2)}$  obtained at the end of Step 2 (Figure 3) by using  $\tilde{\mu}_0 = 10^2$ . The remaining information is the same shown in the caption of Figure 11.

– GEO-XXXX

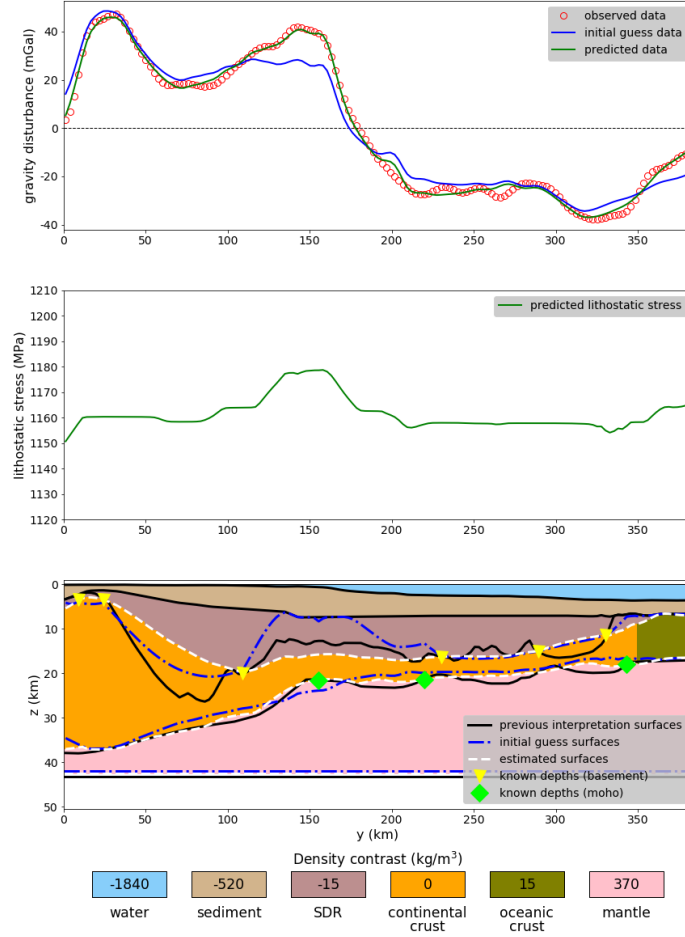


Figure 13: Application to real data on Pelotas basin, Brazil. Estimated model  $\mathbf{p}^{(3)}$  obtained at the end of Step 3 (Figure 3) by using  $\mathbf{p}^{(2)}$  (Figure 12) as initial approximation (dashed blue lines) and  $\sigma = 7$  (equation 23). The remaining information is the same shown in the caption of Figure 11.

– GEO-XXXX

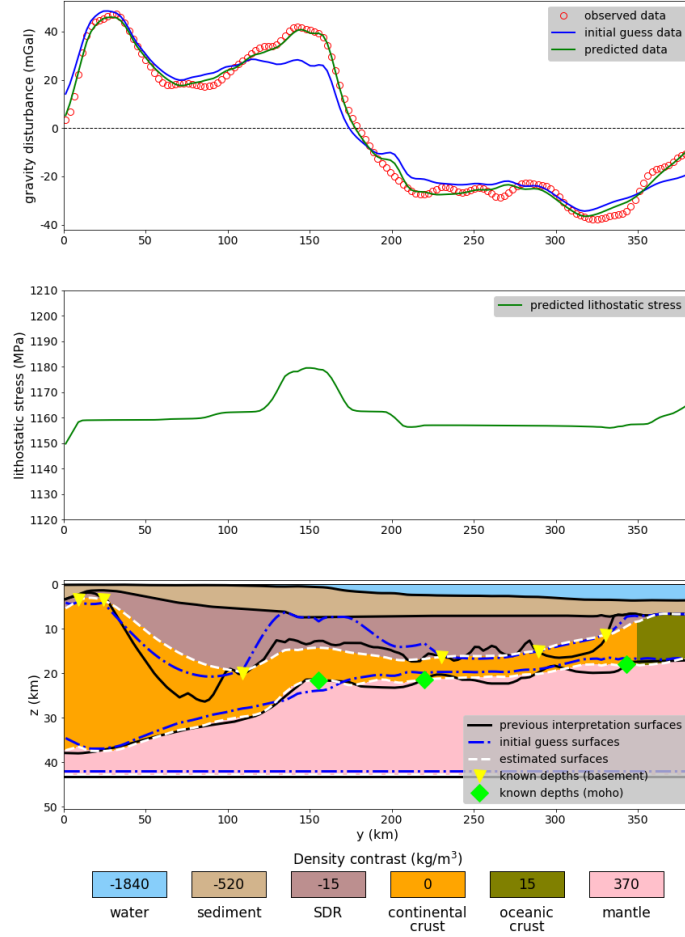


Figure 14: Application to real data on Pelotas basin, Brazil. Estimated model  $\mathbf{p}^{(3)}$  obtained at the end of Step 3 (Figure 3) by using  $\mathbf{p}^{(2)}$  (Figure 12) as initial approximation (dashed blue lines) and  $\sigma = 17.6$  (equation 23). The remaining information is the same shown in the caption of Figure 11.

– GEO-XXXX

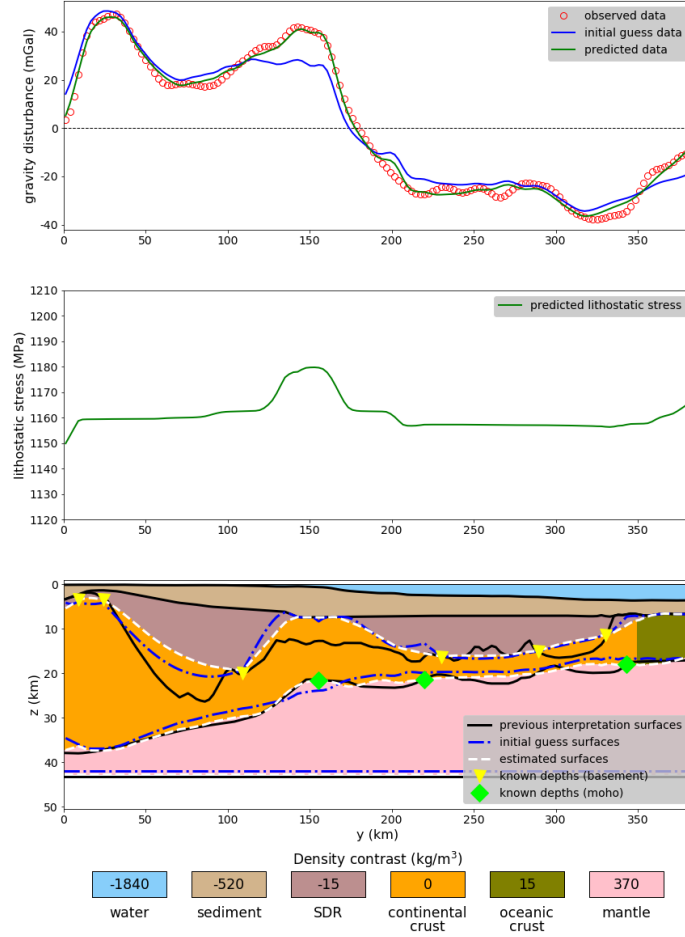


Figure 15: Application to real data on Pelotas basin, Brazil. Estimated model  $\mathbf{p}^{(3)}$  obtained at the end of Step 3 (Figure 3) by using  $\mathbf{p}^{(2)}$  (Figure 12) as initial approximation (dashed blue lines) and  $\sigma = 19$  (equation 23). The remaining information is the same shown in the caption of Figure 11.

– GEO-XXXX



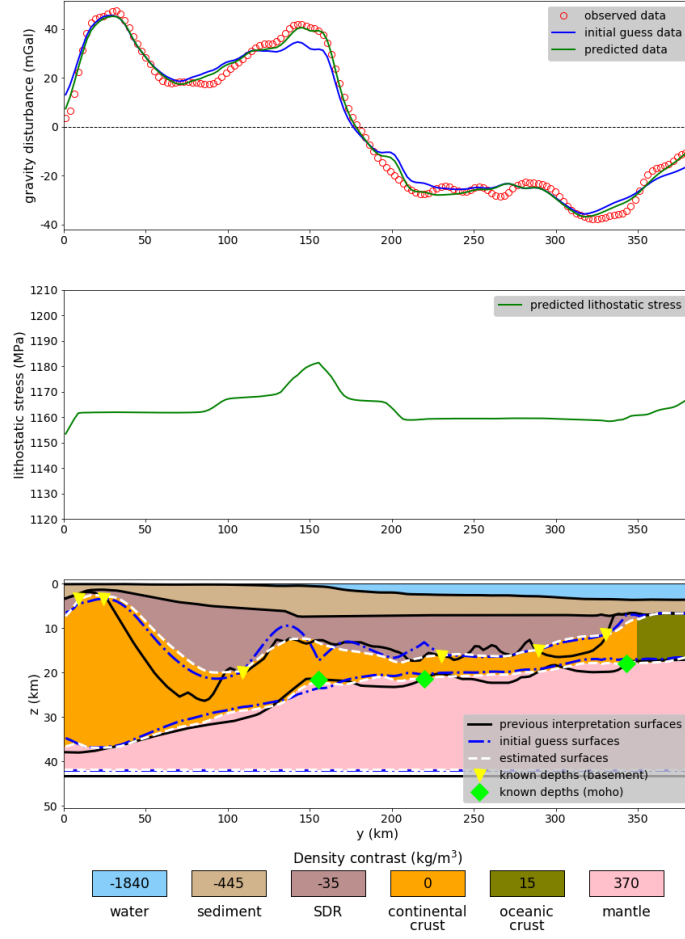


Figure 16: Application to real data on Pelotas basin, Brazil. Alternative estimated model  $\mathbf{p}^{(3)}$  obtained at the end of Step 3 (Figure 3). The differences between this model and those shown in Figures 13, 14 and 15 are the densities  $\rho^{(1)}$  and  $\rho^{(2)}$  attributed to the sediments and SDR (Table 2), as well as the parameter  $\sigma$  (equation 23). In this alternative model,  $\rho^{(1)} = 2425 \text{ kg/m}^3$ ,  $\rho^{(2)} = 2835 \text{ kg/m}^3$  and  $\sigma = 17$ . The remaining information is the same shown in the caption of Figure 11.

– GEO-XXXX